Structural model for the biogenic Mn oxide produced by Pseudomonas putida

Mario Villalobos, Bruno Lanson, Alain Manceau, Brandy Toner, Garrison Sposito

1 **1925R1 (Revision 1)**

2 **Structural model for the biogenic Mn oxide produced by *Pseudomonas putida***

3

4 Mario Villalobos[1,*], Bruno Lanson[2], Alain Manceau[2], Brandy Toner[3], and Garrison Sposito[3]
5

6 [1]Environmental Bio-Geochemistry Group, LAFQA, Instituto de Geografía, National
7 Autonomous University of Mexico (UNAM), Circuito Exterior, Ciudad Universitaria,
8 México, Coyoacán, 04510, D.F., México
9 [2]Environmental Geochemistry Group, LGIT, Maison des Géosciences, BP53, University of
10 Grenoble – CNRS, 38041 Grenoble Cedex 9, France
11 [3]Division of Ecosystem Sciences, University of California at Berkeley,
12 Berkeley, CA 94720-3110, USA
13
14
15 **ABSTRACT**
16
17 X-ray diffraction (XRD) and Mn K-edge extended X-ray absorption fine structure (EXAFS)
18 spectroscopy were combined to elaborate a structural model for phyllomanganates (layer-type
19 Mn oxide) lacking 3D ordering (turbostratic stacking). These techniques were applied to a
20 sample produced by a common soil and freshwater bacterium (*Pseudomonas putida*) and to
21 two synthetic analogs, δ-MnO_2 and "acid birnessite", obtained by the reduction of potassium
22 permanganate with $MnCl_2$ and HCl, respectively. To interpret the diffraction and
23 spectroscopic data, we applied an XRD simulation technique utilized previously for well-
24 crystallized birnessite varieties, complementing this approach with single-scattering-path
25 simulations of the Mn K-edge EXAFS spectra. Our structural analyses revealed that all three
26 Mn oxides have an hexagonal layer symmetry with layers comprising edge-sharing $Mn^{4+}O_6$
27 octahedra and cation vacancies, but no layer $Mn^{3+}O_6$ octahedra. The proportion of cation
28 vacancies in the layers ranged from 6 to 17 %, these vacancies being charge-compensated in
29 the interlayer by protons, alkali metals, and Mn atoms, in amounts that vary with the
30 phyllomanganate species and synthesis medium. Both vacancies and interlayer Mn were

[*]Author to whom correspondence should be addressed (marvilla@igiris.igeograf.unam.mx)

most abundant in the biogenic oxide. The diffracting crystallites contained three to six randomly stacked layers, and have coherent scattering domains of 19-42 Å in the **c*** direction, and 60-85 Å in the **ab** plane. Thus, the Mn oxides investigated here are nanoparticles that bear significant permanent structural charge resulting from cation layer vacancies and variable surface charge from unsaturated O atoms at layer edges.

INTRODUCTION

Manganese 2+ oxidation occurs primarily through biological mediation in the oxic and oxic/anoxic transition zone of aqueous environments (Tipping et al. 1984; Nealson et al. 1988; Tebo 1991; Ghiorse and Ehrlich 1992; Bartlett and James 1993; Wehrli et al. 1995; Tebo et al. 1997, Harvey and Fuller 1998; Tebo and He 1999; Marble et al. 1999; Morgan 2000; Kay et al. 2001). The oxidation products are mainly insoluble Mn^{4+} oxides of the birnessite family (i.e., hydrous phyllomanganates) comprising edge-sharing Mn-O_6 octahedra with high negative permanent structural charge, due principally to vacant cation layer sites, and correspondingly high cation sorption capacities (Chukhrov et al. 1985; Strobel et al. 1987; Drits et al. 1997; Silvester et al. 1997; Lanson et al. 2000; Bilinski et al. 2002). Todorokite, a Mn oxide with tunnel structure, has also been found associated with birnessites in natural settings, but, since the latter are believed to be precursors to formation of the former (Golden et al. 1987; Shen et al. 1993; Tian et al. 1997; Ching et al. 1999; Luo et al. 1999; Feng et al. 2001), todorokite is probably not a direct product of microbial oxidation.

Natural Mn oxides often are poorly-crystalline solids (Tipping et al. 1984; Friedl et al. 1997; McKeown and Post 2001; Bilinski et al. 2002; Manceau et al. 2003, 2004) and rather few structural investigations of them have been performed (Chukhrov et al. 1985, 1989; Manceau

et al. 1992; Gorshkov et al. 1992). Mineralogical techniques that rely on the presence of long-range order, such as X-ray and electron diffraction, have been applied mainly to synthetic analogs of natural birnessites, most often with an enhanced three-dimensional (3D) ordering (Holland and Walker 1996; Drits et al. 1997; Silvester et al. 1997; Lanson et al. 2000, 2002a; Post et al. 2002; Jurgensen et al. 2004). These techniques have revealed the presence of two-layer symmetries, orthogonal ($a > b\sqrt{3}$) as in triclinic Na-birnessite, and hexagonal ($a = b\sqrt{3}$) as in H-birnessite, depending on the predominant origin of the layer charge (Mn^{3+} for Mn^{4+} substitution, or vacant Mn^{4+} sites within the octahedral sheet, respectively). H-birnessite is formed under acidic pH conditions (Silvester et al. 1997). It has the hexagonal unit-cell parameters $a = 4.940$ Å, $b = a/\sqrt{3} = 2.852$ Å, $c = 7.235$ Å, $\alpha = \beta = \gamma = 90^{o}$, with 0.833 Mn ions and 0.167 cation vacancies per layer octahedron, and 0.167 interlayer Mn^{3+} ions located above or below layer vacancies in a triple-corner sharing configuration. The vacancies are long-range ordered, in that they appear in every third row of Mn cations along [100], with half of the Mn sites along these rows being vacant (Drits et al. 1997). Water molecules associated with interlayer Mn cations provide for strong hydrogen bonds between the layers (Lanson et al. 2000).

Villalobos et al. (2003) characterized a set of analogs of natural birnessites showing a limited 3D ordering, including a biogenic Mn oxide produced in culture by a common soil and freshwater bacterium, *Pseudomonas putida*. Based on comparison of their layer symmetry, Mn oxidation numbers, and other physicochemical properties, all of the Mn oxides investigated appeared to be more structurally related to hexagonal H-birnessite than to the triclinic Na-birnessite variety. Also, the biogenic Mn oxide was concluded to have reactive and structural properties intermediate between those of the synthetic **c**-disordered phyllomanganates δ-MnO_2 and "acid birnessite", which are formed through the reduction of

permanganate with $MnCl_2$ or HCl, respectively. More recently, Jurgensen et al. (2004) studied the structure of the Mn oxide produced by another bacterium species (*Leptothrix discophora*) by X-ray absorption fine structure (XAFS) spectroscopy and X-ray diffraction (XRD). They found that this compound consists of single octahedral-layer microcrystals composed of Mn^{4+}, Mn^{3+}, and Mn^{2+} similarly to triclinic Na-birnessite. They also identified the possible location of some Mn octahedra in corner-sharing configuration with those from the layer plane, as in H-birnessite.

The birnessite samples previously studied by Villalobos et al. (2003) appear to have simple layer structures made up almost entirely of Mn^{4+} octahedra, their complexity arising from the presence of layer vacancies and lack of 3D ordering. In the present paper, we extend our previous work with a detailed structural investigation of the same samples using quantitative XRD and extended XAFS (EXAFS) spectroscopy. To interpret the XRD data, we applied a simulation technique utilized previously for birnessites with an enhanced 3D ordering (Manceau et al. 1997; Drits et al. 1998a; Lanson et al. 2000, 2002a, b), complementing this approach with single-scattering-path analyses of Mn K-edge EXAFS spectra.

EXPERIMENTAL METHODS

Synthesis and Characterization of Mn Oxide Samples

The biogenic Mn oxide and its two synthetic analogs were prepared using methods described in Villalobos et al. (2003). Briefly, the biogenic Mn oxide was produced in cultures of *Pseudomonas putida* strain MnB1 provided by Dr. B. M. Tebo (Scripps Institution of Oceanography). Bacteria were grown at 27 ^{o}C to the stationary phase of growth in a liquid

suspension rich in nutrients and in the presence (or absence, for a cell control sample) of total (Mn^{2+}) = 1.0 mM. A sample of the biogenic oxide was cleaned of organic material by gradual iterative oxidation using 0.2 % NaOCl reagent, taking care not to oxidize Mn^{4+} or Mn^{3+} in the sample. δ-MnO_2 was prepared using a "redox" method with stoichiometric amounts of $KMnO_4$ and $MnCl_2$ reagents (Catts and Langmuir 1986; Mandernack et al. 1995; Luo and Suib 1997; Luo et al. 2000). Physicochemical characterization of the sample (Villalobos et al. 2003) indicated a composition exclusively of Mn^{4+} and a highly pH-dependent cation sorption capacity. Acid birnessite was prepared by reducing $KMnO_4$ with concentrated HCl at boiling temperature (McKenzie 1971). The solids were oven-dried overnight at 70 ^{o}C, except for acid birnessite, which was freeze-dried, and a sample of uncleaned biogenic oxide, which was washed, centrifuged, and left as a wet paste for in-situ EXAFS spectroscopy.

Thermogravimetric analyses (TGA) were performed to determine the water content on ca. 20 mg of the dried samples except for the uncleaned biogenic oxide. The weight loss was measured by heating the samples on a Pt tray from room temperature to ca. 250 ^{o}C at a rate of 10 ^{o}C/min (SDT 2960 apparatus from TA Instruments). Alumina powder was used as reference material for weight loss calibrations. Two peaks were obtained in plots of weight/temperature differentials vs. temperature for all samples. They were decomposed using Galactic Grams 32 (vol. 6) software to determine the fractions of loosely bound (removed at < 80 ^{o}C) and strongly sorbed water (retained up to 250 ^{o}C), but excluding structural water bound to interlayer Mn cations. Duplicate analyses per sample were performed and the results obtained were used to constrain the water contents in the XRD simulations. Results are listed in Table 1.

X-ray Diffraction

Dry samples were crushed in an agate mortar, and powder XRD patterns (CuKα radiation, λ = 1.5418 Å) were collected with a Bruker D5000 powder diffractometer equipped with a Kevex Si(Li) solid-state detector. Intensities were measured at 0.04 ^{o} 2θ intervals with 40s counting time per step.

Simulations of XRD patterns were performed following the trial-and-error procedure developed by Drits and Tchoubar (1990) and applied previously to both natural and synthetic birnessites (Chukhrov et al. 1985; Manceau et al. 1997; Drits et al. 1998a; Lanson et al. 2000, 2002a, 2002b). Details on the programs used to simulate XRD patterns and on the fitting procedure are given by Drits and Tchoubar (1990), Drits et al. (1998a), and Plançon (2002). As the main features of XRD profiles recorded for the three samples resemble those reported by Drits et al. (1997) for turbostratic birnessite, the experimental patterns were divided for the simulations in two angular domains containing different families of reflections. In the low-angle region (5-30 ^{o} 2θ CuKα – d-spacing >10 to 3.0 Å), 00*l* reflections were calculated to assess the validity of the lamellar structure proposed by Villalobos et al. (2003) for the synthetic oxides. In addition, the simulation of 00*l* reflections allowed quantification of the extent of coherent scattering domains (CSDs) along the axis perpendicular to the **ab** plane (**c*** axis) using a lognormal distribution of CSD sizes parameterized by an average number of layers (N_{Av} – Drits et al. 1998b). In the high-angle range (32-75 ^{o} 2θ CuKα – *d*-spacing 2.80-1.27 Å), the 20*l*,11*l* and the 02*l*, 31*l* reflections (Miller indexing based on a C-centered unit cell) were calculated to determine the structure of both the octahedral layer and the interlayer region (atomic coordinates and occupancies of the different sites). CSDs in the **ab** plane were assumed to have a disk-like shape whose average radius was constrained by fitting the first of

the two high-angle maxima. For all samples, the background was assumed to decrease linearly over the angular range considered. The average Mn oxidation number along with the alkali metal and structural water content of the samples were used to constrain initial assumptions about the stoichiometry of interlayer species in the simulations. Quality of fit was assessed over the 34-75 ° 2θ CuKα range assuming the commonly employed R_{WP} factor, and comparing it to the statistical error associated with measured intensities (R_{Exp}) (Howard and Preston 1989).

EXAFS Spectroscopy

Manganese K-edge EXAFS spectra were measured at room temperature on wiggler beamline 4-3 at the Stanford Synchrotron Radiation Laboratory in transmission mode. A Si(220) crystal pair was used to create monochromatic X-rays and a Pt-coated mirror was used to reject harmonic X-rays. A 1-mm vertical entrance slit located 17.2 m from the source was used to improve the energy resolution by reducing the beam divergence on the monochromator. Dry Mn oxide samples were mixed with $LiCO_3$ [Mn oxide:$LiCO_3$ (w/w) ≈1:10], to ensure an absorbance of the edge jump of 1 to 1.5, then mounted on 1-mm thick Teflon holders in 25 mm x 3 mm slots. Raw biogenic oxide with cellular material was centrifuged and mounted directly as wet paste into these holders. Samples were held in place with Kapton tape X-ray windows. Spectra were acquired over the energy range 6400 to 7400 eV, with typically two to three runs per sample performed, each run taking approximately 30 min. Either a permanganate solid (Mn^{7+}) (absorption edge jump at 6543 eV set at the maximum of the first derivative of the edge) or a Mn metal foil (absorption edge jump at 6539 eV) were used to calibrate the monochromator before every sample run. No beam-induced changes in Mn oxidation state were observed.

The EXAFS data analysis was performed in the single-scattering approximation using home-made software for data normalization and Fourier transformation, and WinXAS (Ressler 1998) for spectral simulations. Fourier transformations were done on the entire $k^3\chi(k)$ curves shown in the Results section with a Kaiser-Bessel window ($\tau = 3$). Transformation from reciprocal (*k*) to real (R) space produces radial structure functions (RSFs) with peaks corresponding to average absorber-backscatterer distances, but deviating from the true R distance by ΔR due to a phase shift. Spectral simulations were performed on Fourier-filtered data using Mn-O and Mn-Mn phase shift and amplitude functions calculated with FEFF v. 7 (Zabinsky et al. 1995) for the λ-MnO_2 reference (Thackeray et al. 1993). The Mn-O and Mn-Mn Feff files were tested on the spectrum of the reference, and good agreement was found between EXAFS and crystallographic values. ΔE, the difference between the experimental (taken to be the half-edge jump point) and theoretical origins for the energy scale (E), was treated as a single adjustable parameter for all sets of backscattering atoms, and S_0^2, the amplitude reduction factor, was calibrated using λ-MnO_2. Since the EXAFS analysis in the present work is limited to single-scattering-path calculations, any interpretation of long distance Mn-Mn pairs shells ($R + \Delta R > 3.5$ Å), which requires full multiple-scattering calculations, is semi-quantitative. Below this distance, multiple scattering (MS) contributions are negligible (see Figure 15 of Manceau et al. 1998).

RESULTS AND DISCUSSION

XRD Patterns

Figure 1 shows a maximum of four major XRD peaks for the Mn oxide samples studied, whose positions and relative intensities closely resemble those reported by Drits et al. (1997)

206 for turbostratic birnessite. From this positive comparison it is possible to hypothesize that the
207 two peaks occurring at ~7.3-8.0 Å and 3.6-3.8 Å correspond to 001 and 002 basal reflections,
208 although they do not strictly define a rational series. In addition, these reflections are
209 significantly shifted as compared to the positions of 00l reflections commonly reported for
210 birnessite samples. The two peaks observed at higher angles (2.42 - 2.44 and 1.41 - 1.42 Å)
211 likely correspond to 20,11, and 02,31 bands, respectively, choosing a C-centered layer cell.
212 The ratio of the *d* values of the two bands (1.720 - 1.725) is close to the 1.732 = $\sqrt{3}$ value
213 expected for layers having a hexagonal symmetry. These bands do not show significant
214 modulations of the *hkl* reflections and instead exhibit a strong asymmetry on their high-angle
215 side. This profile shape is characteristic of lamellar compounds with a turbostratic stacking,
216 i.e., lacking well-defined displacement/rotation between successive layers (Brindley and
217 Brown 1980). A broad "hump" is however visible at ca. 50-55 ° 2θ CuKα for all three
218 samples (Figure 1). In comparison to the acid-birnessite (Fig. 1a), the first two maxima at ~8
219 and 3.8 Å for δ-MnO_2 are broadened (Fig. 1b), and also significantly shifted relative to their
220 ideal positions for a "7 Å" lamellar compound. The broadening of the basal reflections of δ-
221 MnO_2 extends to the 20,11 and 02,31 bands, and the broad "hump" between 50 and 55° 2θ
222 CuKα has a different shape from that of the acid birnessite pattern. The two low-angle
223 maxima of the pattern for the biogenic oxide are at ~7.6 and 3.8 Å, and have a shape
224 intermediate between those of the two previous samples (Fig. 1c). The biogenic oxide pattern
225 exhibits an additional shoulder on the low-angle side of the 3.8 Å maximum. This shoulder
226 arises from the contribution of dead cells to the diffracted intensity, as shown on the XRD
227 pattern from the bacteria alone (Fig. 1d). The admixture of bacterial cells does not modify
228 significantly the pattern from the biogenic oxide component in the high-angle region. The
229 two 20,11 and 02,31 bands are still observed for the biogenic oxide, but the high-angle tail of

230 the former is less pronounced than in the two other samples, and the hump is slightly shifted
231 to higher 2θ values.
232
233 **Simulations of the Low-Angle Region (5-30°2θ CuKα)**
234
235 One objective of these simulations was to verify if the observed non-rationality and the
236 significant positional shift of the two diffraction maxima observed in this low-angle range
237 was related to the small dimensions of the CSDs along the **c*** direction as described by Drits
238 and Tchoubar (1990) for layer silicates. Calculations were performed assuming a lamellar
239 structure for all three oxides considered. Elementary birnessite layers consist of the sheet of
240 Mn octahedra itself, which possibly contains vacant layer sites, and of associated interlayer
241 species, which include interlayer Mn and alkali cations and coordinated H_2O molecules (see
242 Equation 1 below). Atomic coordinates along the **c*** direction were equal to those
243 determined from the analysis of *hkl* bands. Upon fixing these values, the amplitude, width,
244 and position of the experimental diffraction peaks in this region essentially depend on the size
245 of the CSDs along **c*** and, therefore, on the number of layers in the diffracting crystallites.
246 Although the fits to the experimental data are not perfect, the main features of the diffraction
247 patterns were fairly reproduced by the simulations (Fig. 2). In particular, for all three samples
248 the calculated positions, widths, and relative intensities were similar to the experimental data,
249 thus providing strong support for the assumed lamellar structure of the unknowns (Villalobos
250 et al. 2003). For the biogenic sample, the scattering from dead bacterial cells was not
251 included in the calculation and, hence, only the high-angle contribution of the 002 peak was
252 reproduced. The average sizes of the CSDs estimated from the models equal 2.6 layers (~1.9
253 nm) for δ-MnO_2, 2.8 layers (~ 2.0 nm) for the biogenic oxide, and 5.8 layers (~4.2 nm) for the
254 acid birnessite (Table 2).

255

256 **Simulations of the high-angle region (>30°2θ CuKα)**

257

258 The successful simulation of the low-angle peaks supports our indexing of the high-angle
259 reflections as 20,11 and 02,31 bands. As compared to equivalent reflections for hydrous
260 layer silicates (Manceau et al. 2000a,b), the profiles of the 20,11 reflections are modulated
261 and their shapes are different from one sample to another, indicating a variation of the
262 structure factors, and hence of the sample structures. As will be shown below, these
263 modulations can be used to determine both the layer and interlayer structures of the
264 phyllomanganate samples despite the absence of any 3D ordering.
265 For all simulations the generic structural formula,

266

267 $$H_a(Na,K)_bH_2O_cMn^{3+,2+}{}_{tc}[Mn^{4+}{}_d,vac_e]O_2 \qquad (1)$$

268

269 was assumed, where interlayer species are written to the left of the square brackets and tc
270 refers to interlayer Mn in triple corner-sharing positions above or below cation vacancies
271 (vac) in the layer (enclosed in square brackets, except for the oxygens). The stoichiometric
272 coefficients were calculated from the average Mn oxidation number and the alkali metal
273 content determined previously (Villalobos et al. 2003), and from the water content
274 determined by TGA (Table 1). Parameters refined in the XRD simulations include the unit-
275 cell dimensions in the **ab** plane, from the position of the two high-angle maxima, and the
276 amount of vacant layer sites, the amount and position of interlayer Mn cations, the positions
277 of interlayer alkali cations and of associated H_2O molecules, and the size of the CSDs in the
278 **ab** plane. All sample spectra were simulated assuming an hexagonal layer symmetry and
279 choosing a C-centered unit-cell with parameters $b = 2.838$ Å, $a = b\sqrt{3} = 4.916$ Å, $\gamma = 90°$, and

a basal *d*(001) distance of 7.20 Å. No parameters were used to define the layer-stacking mode, as layer stacking is random with W_R, the occurrence probability of random displacement/rotation between adjacent layers, being equal to 100 %. Optimal parameters obtained from the simulations are listed in Tables 2 and 3, and selected interatomic distances are reported in Table 4.

δ-MnO_2. Since the average Mn oxidation number measured for this oxide is 4.0 (Table 1), the layer charge deficit was assumed to arise only from vacant layer sites. The optimal model had 6 % octahedral vacancies and did not contain interlayer Mn (tc = 0). Accordingly, the layer charge deficit was compensated by interlayer Na, whose fraction was constrained to be four times the refined fraction of vacant layer sites. The amount of interlayer H_2O was assumed to be three times the amount of interlayer Na (Post and Veblen 1990), leading to a water content (12.7 %) consistent with the TGA value (15.8 %), although somewhat smaller. Thus, the structural formula corresponding to the optimum fit shown in Figure 3a (R_{WP} = 10.7 %, R_{EXP} = 3.5 %) is:

$$Na_{0.24}(H_2O)_{0.72}[Mn^{4+}_{0.94},vac_{0.06}]O_2 \quad (2)$$

The coordinates of Na and H_2O are (0.225, 0, 1/2) (Table 3a – Fig. 4) and the distance between water molecules and nearest layer oxygen atoms (O_{layer}) is 2.65 Å, which is favorable to the formation of strong H-bonds (Table 4).

Acid Birnessite. The average Mn oxidation state of slightly lower than 4.0 (Table 1) suggests the occurrence of Mn^{3+} cations, most likely above/below vacant layer sites, since the layer has an hexagonal symmetry. Thus, the amounts and positions of interlayer Mn were

optimized during the simulations, together with the amount of octahedral vacancies. The amount of interlayer H_2O was linked to that of alkali cations, as for the δ-MnO_2 simulation, and their positions were also optimized. The refined structural formula, which yielded the optimum match between the calculated scattering profile and data shown in Figure 3b (R_{WP} = 9.3 %, R_{EXP} = 2.8 %), is:

$$H_{0.06}K_{0.18}(H_2O)_{0.54}Mn^{3+}_{0.08}(H_2O)_{0.24}[Mn^{4+}_{0.88},vac_{0.12}]O_2 \quad (3)$$

This sample has a higher amount of vacant layer sites (0.12 per octahedron) than δ-MnO_2, and only two-thirds of the octahedral vacancies (0.08 per octahedron) are capped on one side by octahedrally coordinated interlayer Mn^{3+} cations (Fig. 4). The stoichiometric coefficient of Mn^{3+} is about half that of H-birnessite (Lanson et al. 2000). The average Mn oxidation degree (3.92) determined by XRD agrees fairly well with the value determined by wet chemistry (3.96 ± 0.02 – Villalobos et al. 2003), which provides confidence in the overall consistency of our structural approach. The remaining layer charge is balanced by interlayer K^+ cations and protons (0.18 and 0.06 per octahedron, respectively), the alkali metal content (K/Mn = 0.19) being consistent with the K/Mn molar ratio measured by wet chemistry (0.20 ±0.008 – Villalobos et al. 2003). The amount of structural water (9.6 %) is consistent with the TGA value (7.5 % – Table 1), although somewhat larger. The position of the water molecules (0.200, 0.0, 0.5 – Table 3b) is close to that determined for δ-MnO_2 (0.225, 0.0, 0.5), and again leads to a short $<H_2O\text{-}O_{layer}>$ distance (2.68 Å) that is favorable to the formation of strong H-bonds with O_{layer}. However, the assumption of a common position for K^+ and H_2O did not yield optimal fits to the XRD pattern (R_{wp} = 10.3 %). Best agreement between calculation and experiment was obtained with K^+ at (-0.203,0.0,0.5), which is above or below empty tridentate cavities of the layer surface at 2.97 Å from O_{layer}. K atoms are

330 slightly shifted in the **ab** plane from the center of the cavity in the direction of the nearest
331 O_{layer}-O_{layer} edge of the Mn layer (Fig. 4). This position is close to that refined by Gaillot et
332 al. (2003) (-0.229, 0.0, 0.5) for a birnessite single crystal having 11 % octahedral vacancies,
333 of which two thirds were capped on one side by Mn^{3+} cations. The similar layer and interlayer
334 structures found in the disordered birnessite synthesized at room temperature and in the single
335 crystal form synthesized at 800°C suggest common structural principles despite the differing
336 conditions of formation of the two species.
337
338 **Biogenic Oxide**.
339 As noted above, X-ray scattering from bacterial cells does not produce any significant
340 modulations of the diffracted intensity over the analyzed angular range (Fig. 1d) and,
341 consequently, all experimental features were interpreted as arising from the manganate
342 admixture. As compared to the two previous samples, this oxide has an even lower Mn
343 oxidation state (3.90 ±0.05 – Table 1), thus suggesting a higher content of interlayer Mn, and
344 possibly also of octahedral vacancies. Also, this sample has a lower alkali/Mn ratio (0.167
345 ±0.003), which suggests a higher proportion of vacant layer sites capped by interlayer Mn.
346 Accordingly, the optimum fit to the XRD pattern of this oxide (Fig. 3c – R_{WP} = 9.8 %, R_{EXP} =
347 3.1 %) was obtained for the following structural formula:
348
349 $$H_aNa_{0.15}(H_2O)_{0.45}Mn^{2+,3+}{}_{0.167}(H_2O)_{0.50}[Mn^{4+}{}_{0.833},vac_{0.167}]O_2 \quad (4)$$
350
351 The amounts of vacancies and interlayer Mn are identical (0.167 per octahedron), and the
352 same as in H-birnessite (Lanson et al. 2000). However, the short <Mn-O_{layer}> distance (1.92
353 Å – Table 4) pleads for the sole presence of Mn^{4+} within the octahedral layers in contrast to
354 H-birnessite. In the optimized structural model, octahedrally coordinated interlayer Mn

355 atoms are slightly farther from the layer surface (*z*-coordinate = 2.15 Å – Table 3 c) than in
356 the other birnessite samples, including H-birnessite (*z*-coordinate = 2.10 Å – Tables 3a, b –
357 Lanson et al. 2000). This position results in a $<Mn_{interlayer}\text{-}O_{layer}>$ distance of 2.00 Å, that is
358 significantly longer than usual (1.98 Å). This increase in distance is consistent with the likely
359 presence of interlayer divalent Mn cations in the biogenic oxide. The residual layer charge is
360 balanced by interlayer Na^+ cations (0.15 per octahedron) and protons, the amount of which
361 depends on the actual valency of interlayer Mn cations. The amount of interlayer Na
362 estimated from our XRD model is consistent with the Na/Mn molar ratio (0.167 ± 0.003)
363 reported by Villalobos et al. (2003), and the amount of water bound to Na (8.2 %) is slightly
364 smaller than the TGA value (10.0 %). Finally, the optimized atomic coordinates for Na and
365 H_2O are similar to those obtained for δ-MnO_2, leading again to meaningful $<H_2O\text{-}O_{layer}>$ and
366 $<Na\text{-}O_{layer}>$ distances.
367
368 **Sensitivity of Calculated XRD Patterns to Structural Parameters**. As the optimum fits to
369 the experimental data were obtained using a trial-and-error approach (making the assessment
370 of uncertainties very difficult), the actual sensitivity of the XRD simulations to key structural
371 parameters needs to be assessed. The sensitivity to the position of interlayer species will be
372 illustrated by taking δ-MnO_2 as a case study. The optimum positions of Na and H_2O [(0.225,
373 0.0, 0.5) and equivalent positions] are labeled "O3" in Figure 4 . Placing the two interlayer
374 species above or below an empty layer octahedron [position (0.0, 0.0, 0.5) – Alt. 1 in Fig. 4]
375 modified the XRD profile considerably, especially the 20,11 band (Fig. 5a – R_{WP} = 21.9 %).
376 Even a small shift of these "light" species from their optimum (0.225, 0.0, 0.5) position to
377 (0.333, 0.0, 0.5) (position "Alt. 2" in Fig. 4) changed significantly the calculated XRD profile
378 relative to the best simulation (Fig. 5b – R_{WP} = 12.2 %). Finally, when interlayer species are
379 sitting above/below the tridentate cavities [Position "Alt. 3" in Fig. 4 with coordinates (-

380 0.167, 0.0, 0.5)], the calculated 20,11 band was broadened and differed greatly from
381 experimental data (Fig. 5c - R_{WP} = 24.1 %).
382 Figure 6 illustrates the sensitivity of the calculated XRD profiles to the mean radial
383 dimension of the CSDs in the **ab** plane, taking again δ-MnO_2 as an example. In Figure 6a,
384 this dimension has been increased from 6.0 nm, the optimum value (Table 2), to 10.0 nm. As
385 a result, the 20,11 band peaks at lower 2θ value. In addition, the calculated band is sharper,
386 leading to a poorer reproduction of the experimental profile (R_{WP} = 15.0 %). An opposite
387 effect is observed when the mean CSD radial dimension is decreased from 6.0 to 3.0 nm (Fig.
388 6b – R_{WP} = 11.6 %). Note that the CSD size does not affect the position of the modulation at
389 about 45 ° 2θ CuKα, which depends only on the layer structure.
390
391 The sensitivity of the calculated XRD profiles to the location and amount of interlayer Mn is
392 illustrated next with the biogenic oxide (Fig. 7). Decreasing the stoichiometric coefficient tc
393 (Equation 1) from its optimum 0.167 value to 0.100 modified the shape of the high-angle
394 "tail" of the 20,11 band in a manner that smoothened the scattering dip at ~ 45 ° 2θ CuKα
395 rendering the calculated hump less pronounced (Fig. 7a – R_{WP} = 11.3 %) relative to the
396 optimum fit (Fig. 3c – R_{WP} = 9.8 %). When both the proportion of interlayer Mn and layer
397 vacancies were decreased from 0.167 to 0.100, the lineshape of the 20,11 band was
398 broadened (Fig. 7b – R_{WP} = 14.6 %). As expected from the high sensitivity of the calculated
399 XRD patterns to the position of "light" interlayer species, demonstrated previously with Na
400 and H_2O in δ-MnO_2, moving interlayer Mn from its optimal position dramatically modified
401 the 20,11 lineshape, as observed when the 0.167 interlayer Mn atoms were located
402 above/below the tridentate cavities (position Alt. 3 – Fig. 4; Fig. 7c – R_{WP} = 25.3 %).
403

404 **EXAFS Spectra**

405

406 The k^3-weighted Mn K-edge EXAFS spectra collected for the samples are shown in Figure
407 8a. Frequencies for all the Mn oxides studied were similar, with differences between the
408 samples arising mostly in the amplitudes. These amplitude differences are also evident in the
409 corresponding radial structure functions (RSFs, uncorrected for phase shifts) shown in Figure
410 8b. The uncleaned biogenic oxide sample shows a somewhat distinctive behavior at low *k*
411 values (Fig. 8a). These effects are probably a contribution of a relatively important Mn^{2+}
412 fraction (16-19 mole %) in this sample, which is absent from the others (Villalobos et al.
413 2003).

414

415 The RSFs exhibit two principal peaks at similar interatomic distances for all samples (Fig.
416 8b), including the uncleaned biogenic oxide. From a qualitative comparison with previously-
417 reported spectra for layer type Mn oxides, it can be concluded that these two peaks arise
418 mainly from single-scattering photoelectron interactions in the first Mn-O shell and in the
419 second Mn-Mn shell, respectively (Manceau and Combes 1988; Manceau et al. 1992b;
420 Silvester et al. 1997). Differences among the samples are observed mostly in the peak
421 amplitudes, particularly for the Mn-Mn peak, and in the small feature that appears just
422 beyond this peak at ca. $R+\Delta R$ of 3 Å. This feature was used to elucidate important structural
423 differences between the Mn oxides using single-scattering ab initio FEFF simulations.
424 Specifically, the presence of a shoulder or a distinctive peak at $R+\Delta R$ ~3 Å for the uncleaned
425 biogenic oxide may be indicative of Mn octahedra in different configurations from the edge-
426 sharing octahedra in the layers, e.g. triple-corner (TC) sharing octahedra, as observed in H-
427 birnessite and chalcophanite (Silvester et al. 1997) and in tectomanganates (Manceau and
428 Combes 1988).

The EXAFS spectrum of the clean biogenic oxide clearly shows a shift in the $\chi(k)$ frequencies in the region between 6 and 8 $Å^{-1}$ (Fig. 8a.), which manifests itself in the disappearance of the feature at R+ΔR ~3 Å in real space (Fig. 8b). This spectral feature is very similar to that seen in the spectra of δ-MnO_2 (Fig. 9) and acid birnessite (Fig. 10). In contrast, the spectrum for the unclean biogenic sample shows a strong similarity to that for H-birnessite, especially in the region between 6 and 7 $Å^{-1}$ (Fig. 11a) and at R+ΔR ~3 Å (Fig. 11b – feature C). Therefore, qualitatively, one may conclude that the biogenic sample as it is synthesized by the bacteria most likely contains interlayer Mn, in similar configuration to H-birnessite.

The peak caused by the third Mn layer shell at R+ΔR ~5.2 Å (Fig. 11b, feature D) is more intense than the peak of the second Mn layer shell at R+ΔR ~4.5 Å, although the two shells comprise six Mn atoms. The magnification of peak D has been attributed to a "focusing effect" between aligned cations in layer type metal oxides (O'Day et al. 1994).

Simulations of the EXAFS Spectra

δ-MnO_2. This layer Mn oxide appears to have a simple structure (Fig. 8) arising from the homogeneity of its Mn oxidation state (Villalobos et al. 2003). The FEFF simulations of the $k^3\chi(k)$ data filtered in the 1.0 < R+ΔR < 3.1 Å interval are shown in Figure 12a and the corresponding optimized parameters are listed in Table 5. The first two shells correspond to Mn-O and Mn-Mn distances of 1.90 Å and 2.87 Å, respectively. The edge-sharing configuration of the Mn^{4+} octahedra (six shared edges per octahedron) is isostructural with that in bivalent metal hydroxides of the brucite [$Mg(OH)_2$] group, including pyrochroite [$Mn(OH)_2$]. To reconcile the interatomic distances obtained by FEFF simulation with this

454 configuration in a crystallographic model, the Mn^{4+} octahedra must flatten slightly. To
455 ensure a Mn-Mn distance of 2.87 Å between adjacent octahedra while keeping all Mn-O
456 distances equal to 1.90 Å, the O-O distance along shared edges must shorten to 2.49 Å (Fig.
457 13, inset). The O-O distances along the unshared edges in this configuration are effectively
458 equal to the interatomic Mn-Mn distance of 2.87 Å.
459
460 An idealized octahedral sheet for δ-MnO_2 may now be constructed (Fig. 13) in which all Mn
461 near neighbor distances are determined by geometry alone. For example, a second O shell
462 [O(2)] is expected at 3.45 Å, and further Mn layer shells are expected at 4.97 Å (dotted lines
463 in Fig. 13) and 5.74 Å. The O(2) shell at 3.45 Å from Mn is within the range of influence of
464 the edge-sharing Mn shell [Mn(1)], and of the triple-corner sharing Mn shell [Mn(tc)], when
465 present, and, consequently, it was included in the spectral fits for all sample spectra.
466 However, spectral simulations showed that adding the Mn-O(2) electronic wave improves the
467 fit in the 4-6 $Å^{-1}$ *k* interval but does not modify significantly the EXAFS parameters from the
468 Mn(1) and Mn(tc) shells because these shells have a maximum amplitude at higher *k*
469 (Manceau and Combes 1988; Schlegel et al. 2001).
470
471 According to the ideal hexagonal layer model of δ-MnO_2, and in the absence of
472 configurations other than edge-sharing octahedra, six near neighbors of Mn centers are
473 expected for all shells (Fig. 13). The optimized fit for the O(1) shell indeed yielded *N* very
474 close to 6 (Table 5). However, the Mn(1) shell fit produced a considerably lower value of *N*,
475 even when taking into account the commonly accepted precision of 20 % in this parameter.
476 Two factors may predominate in causing this reduction: vacant cation sites (i.e., the absence
477 of some Mn near neighbors per Mn center present) and the contribution of particle-edge

478 octahedra that have an incomplete shell of near neighbors, a contribution that is important
479 because of the small size of the layers in our samples.
480
481 Based on a Mn-Mn(1) distance of 2.87 Å as obtained from analysis of the first Mn shell
482 (Table 5), and on a layer size estimate from our XRD simulations of δ-MnO_2 (from the
483 coherent scattering domain radial dimensions – Table 2), a rough estimate of the contribution
484 of layer-edge octahedra may be performed: one sheet of a square particle of dimensions 85 ×
485 85 $Å^2$ yields a total of $(85/2.87)^2 = 900$ octahedra, of which $4 \times (85/2.87) = 120$ occur at the
486 edges. The latter represents 13 % of the total. Assuming smooth edges, we estimate that ca.
487 4 Mn near-neighbors occur for every edge octahedron (Fig. 13). Thus the average number of
488 nearest Mn neighbors for all Mn atom centers in the 85 × 85 $Å^2$ particle is about $0.13 \times 4 +$
489 $(1\text{-}0.13) \times 6 = 5.74$; i.e., a reduction of less than 5 % from the ideal value. Therefore, the low
490 coordination number (28 % difference) observed by EXAFS spectral fitting must be due
491 primarily to the presence of vacant Mn sites. Unfortunately, the uncertainty of the predicted
492 *N* value by EXAFS is too high to render a useful quantitative estimate of the vacancy content
493 by this method. However, it provides a convincing qualitative explanation for the occurrence
494 of Mn *N* values significantly lower than the theoretical value of 6 (Fig. 13).
495
496 **Hexagonal birnessite with an Enhanced 3D Ordering.** The H-birnessite (HBi) studied by
497 Silvester et al. (1997) has a more complex structure than δ-MnO_2 because of the presence of
498 significant Mn^{3+} in the layer and at interlayer sites in TC octahedra above cation vacancies.
499 The significant increase by 0.01 Å of the Mn-Mn(1) distance relative to δ-MnO_2 (Table 5) is
500 indicative of the presence of Mn^{3+} in the layer, whereas the Mn shell at 3.49 Å with an
501 effective coordination number of 2.8 is characteristic of corner-sharing linkages between
502 layer and interlayer octahedra.

503

504 **Acid Birnessite**. As expected from the average Mn oxidation number of 3.96 for this oxide
505 (Villalobos et al. 2003) and from the RSF (Fig. 8b) and XRD data, FEFF simulations gave
506 optimized structural parameters very similar to those for δ-MnO_2 (Fig. 12b, Table 5). The
507 main difference between the two structures lies in the larger size of the diffracting crystallites
508 (CSD) in acid birnessite.

509

510 **Biogenic Oxide**. Simulation of the NaOCl-cleaned sample of the biogenic oxide produced
511 shells and optimized structural parameters different from the uncleaned sample (Fig. 14), but
512 very similar to those of δ-MnO_2 and acid birnessite (Figs. 9, 10, 12c, Table 5). Figures 11a
513 and 15a show that HBi has a higher wave frequency than the biogenic oxide, which translates
514 in real space to a shift to higher R+ΔR values of peaks B and D (Fig. 11b). Accordingly,
515 Table 5 shows that the Mn-Mn(1) distance is greater by 0.02 Å in HBi. This is due to the
516 presence of layer Mn^{3+} in the latter, and its absence in the biogenic oxide. Matching the
517 simulation of HBi (Fig. 15b), the prominent shoulder at ca. 3 Å in the RSF of the uncleaned
518 sample (peak C in Fig. 11b) was successfully simulated with a TC Mn shell at 3.49 Å (Fig.
519 15c, Table 5). The oxidation state of this interlayer Mn species is different in the biogenic
520 oxide [Mn^{2+}] from that in HBi [Mn^{3+}], however, the Mn-Mn(tc) EXAFS distance is the same
521 for both (Table 5). This may be explained as a trade-off between the larger radius of Mn^{2+}
522 compared to Mn^{3+}, and the need for Mn^{2+} to approach the layer at a closer distance to
523 compensate for a similar negative layer charge. This type of behavior has been reported in
524 chalcophanite, in which Zn is octahedrally-coordinated but has Zn-O_{layer} distances
525 characteristic of a tetrahedral coordination owing to the lowering of the Zn position in the
526 direction of the layer (Wadsley 1955).

527

528 Additionally, note that *N* predicted for the O(1) shell of both is lower than for the other
529 samples (Table 5). This difference occurs because the high proportion of low-valent Mn in
530 the sample causes a higher disorder in the Mn-O EXAFS frequency, manifested in a decrease
531 from what would be observed for pure Mn^{4+}-O pairs. This situation is illustrated in Figure
532 16, which shows an EXAFS simulation for a hypothetical system consisting of 80 % Mn^{4+}-O
533 and 20 % Mn^{2+}-O pairs. In such a system, the frequency of the shorter Mn^{4+}-O pair
534 dominates the EXAFS spectrum (Fig. 16a) and, therefore, the RSF peak for the composite
535 Mn valency spectrum appears at the same distance as that for the pure Mn^{4+} spectrum, but
536 with a lower amplitude (Fig. 16b).
537
538 **General Discussion**
539
540 **Ability of the trial-and-error XRD modeling approach to determine the structure of**
541 **turbostratic compounds**. The ability of the trial-and-error approach used in the present
542 study to unravel the structure of defect-bearing compounds has been amply demonstrated in
543 recent studies of different birnessite varieties with an enhanced 3D ordering (Manceau et al.
544 1997; Drits et al. 1998a; Lanson et al. 2000, 2002a, b; Gaillot et al. 2003, 2004). Based on
545 the above fits to the experimental data and the subsequent sensitivity analysis, it is clear that
546 this trial-and-error approach can also be applied to build meaningful structure models for
547 extremely defective (turbostratic stacking – 100 % of random stacking faults) layered
548 compounds. The symmetry and cation occupancy of the octahedral layer, and to some extent
549 the amounts and positions of interlayer species, were well constrained. Specifically, it was
550 possible to assess the presence and the number of interlayer Mn cations associated with
551 vacant layer sites, and to determine their position with a reasonable precision (e.g., Figs. 3c
552 and 7). The position and, to a lesser extent, the amount of "light" interlayer species, such as

553 Na^+ and H_2O molecules, were also obtained by this approach (e.g., Figs. 3a and 5). Our
554 modeling procedure also provided estimates of the CSD sizes in the **ab** plane for these
555 compounds (e.g., Figs. 3a and 6).
556 The high sensitivity of XRD profiles to the structure of highly defective phyllomanganates
557 contrasts with the limited effect reported previously for other layered compounds having a
558 turbostratic stacking, such as smectites. For example, Manceau et al. (2000a,b) used a similar
559 modeling approach to determine average cation occupancy in nontronite for which the layer
560 and interlayer structures were reasonably well known, a few parameters being left to refine.
561 For this purpose these authors used the relative intensities of 02,11 and 20,13 bands because
562 no modulations were observed for the two diffraction bands. For turbostratic layer
563 compounds, calculated XRD patterns hold information only on the structure of the layer,
564 including interlayer species, and give an estimate of the lateral extension of these layers.
565 However, no information is provided on the layer stacking mode, which is assumed to be
566 totally random. In the present case, modulations of the two *hkl* bands, and especially of the
567 20,11 band, were observed and successfully reproduced by computation assuming a
568 turbostratic stacking. As the position and profile of the bands depend on the amount and
569 atomic coordinates of both layer and interlayer species, they may be used for structural
570 chemistry determination. Similar modulations can result from the partial ordering of the layer
571 stacking (e.g., Ben Brahim et al. 1983; Ben Brahim et al. 1984; Drits & Tchoubar 1990; Viani
572 et al. 2002). Special attention should thus be paid to the structural interpretation of these
573 modulations, and, in this respect, verifying the structural XRD model with independent data
574 from another structural technique, such as EXAFS spectroscopy, is always warranted.
575
576 **Particle size considerations.** The small coherent scattering dimensions obtained from XRD
577 simulations provided estimates for the size of the diffracting crystallites in the nanometer

578 range. The implications of this small particle size include the exposure at the surface of a
579 large proportion of the total structure. Therefore, edge surface sites, which contain
580 unsaturated singly- and doubly-coordinated oxygen groups (Fig. 13), are expected to hold a
581 relatively high proportion of the total particle charge and thus contribute palpably to ion
582 sorption capacity. Other implications of small particle size may be relevant not only to
583 reactivity studies, but also to structural characterization using wet-chemistry and
584 spectroscopic techniques, such as those employed by Villalobos et al. (2003). For example,
585 the molar ratio, [Mn(IV) + vacancies] / O is no longer expected to be 0.5, as in infinitely large
586 octahedral layers. The total charge will depend on both the vacancy content and the number
587 of unsaturated oxygen bonds at the edges of the particles. Small particle size in the radial
588 direction has the potential to create "border effects" that may influence characterization based
589 on spectroscopic techniques that have been calibrated using samples having much larger
590 particle size.
591 **Comparisons between Mn oxides studied.** Complementary information obtained from
592 simulations of XRD patterns and Mn K-edge EXAFS spectra has led to more accurate
593 determination of the structures of the biogenic Mn oxide and its two synthetic analogs
594 investigated by Villalobos et al. (2003). Hexagonal layer symmetry was established for all
595 three Mn oxides studied, with differences occurring mainly in the number of layer vacancies,
596 in the cation interlayer content, and in particle size (coherent scattering domain radial
597 dimensions and number of randomly stacked sheets per crystallite). The uncleaned sample of
598 the biogenic Mn oxide seems to be structurally related to synthetic HBi, including similar
599 vacancy contents and the presence of low-valency interlayer Mn in TC configuration.
600 However, the biogenic phase's octahedral layer is composed of tetravalent Mn only, in
601 contrast to HBi, but in close similarity with δ-MnO_2 and acid birnessite. Thus, the layer
602 charge originates only from the presence of vacant layer sites. Another characteristic of the

603 biogenic oxide is the presence of Mn^{2+} in the interlayer, whereas HBi has Mn^{3+}, and δ-MnO_2
604 and acid birnessite have no Mn^{2+}. This Mn^{2+} is most likely a remnant of unoxidized Mn^{2+}
605 added to the system initially. A recent X-ray absorption study of the oxidation product of a
606 *Leptothrix* bacterium (Jurgensen et al. 2004) detected both Mn^{2+} and Mn^{3+}in the birnessite-
607 like biogenic oxide, suggesting that Mn^{3+} may be a structural component of certain biogenic
608 oxides. In yet another study on biogenic oxides, Mn^{3+} was detected by Scanning
609 Transmission X-ray Microscopy (STXM) (Pecher et al. 2003; Toner et al. 2004), but this
610 species was assigned an intermediate role in the bacterial oxidation process to Mn^{4+}.
611
612 **Acknowledgments**
613
614 The first author would like to thank Philip N. Ross (Materials Science Divison, Lawrence
615 Berkeley National Laboratory) for use of a TGA-DTA apparatus, and John Bargar for
616 facilitating EXAFS measurements and providing technical assistance at the beamline. The
617 third author expresses gratitude to the Division of Ecosystem Sciences, University of
618 California at Berkeley, for its hospitality during a sabbatical leave visit. This research was
619 funded in part (M.V., B.T., G.S.) by the National Science Foundation, Collaborative Research
620 Activities in Environmental Molecular Science (CRAEMS) program (CHE-0089208) and in
621 part (A. M.) by a LDRD grant through the Advanced Light Source, Lawrence Berkeley
622 National Laboratory. SSRL is a national user facility operated on behalf of the U.S. DOE,
623 Office of Basic Energy Sciences.
624
625 **References cited**
626
627 Bartlett, R.J. and James, B.R. (1993) Redox chemistry of soils. Advances in Agronomy,

628 50, 151-208.

629 Ben Brahim, J., Besson, G., and Tchoubar, C. (1983) Layer succession and water
630 molecules arrangement in a homogeneous two-water layer Na-smectite. 5th Meeting of
631 the European Clay Groups, p. 65-75, Prague.

632 Ben Brahim, J., Besson, G., and Tchoubar, C. (1984) Etude des profils des bandes de
633 diffraction X d'une beidellite-Na hydratée à deux couches d'eau. Détermination du
634 mode d'empilement des feuillets et des sites occupés par l'eau. Journal of Applied
635 Crystallography, 17, 179-188.

636 Bilinski, H., Giovanoli, R., Usui, A., and Hanzel, D. (2002). Characterization of Mn
637 oxides in cemented streambed crusts from Pinal Creek, Arizona, U.S.A., and in hot-
638 spring deposits from Yuno-Taki Falls, Hokkaido, Japan. American Mineralogist, 87,
639 580-591.

640 Brindley, G.W. and Brown, G. (1980). Crystal Structures of Clay Minerals and their X-ray
641 Identification. Mineralogical Society, London.

642 Catts, J.G. and Langmuir, D. (1986). Adsorption of Cu, Pb, and Zn by delta-MnO2:
643 applicability of the site binding-surface complexation model. Applied Geochemistry, 1,
644 255-264.

645 Ching, S., Krukowska, K. S., and Suib, S. L. (1999) A new synthetic route to todorokite-
646 type manganese oxides. Inorganica Chimica Acta 294(2), 123-132.

647 Chukhrov, F.V., Sakharov, B.A, Gorshkov, A.I., Drits, V.A., and Dikov, Y.P. (1985)
648 Crystal structure of birnessite from the Pacific Ocean. International Geology Review,
649 27, 1082-1088.

650 Chukhrov, F.V., Gorshkov, A.I., and Drits, V.A. (1989) Supergenic manganese hydrous
651 oxides, Nauka, Moscow, 208 pp.

652 Drits, V.A. and Tchoubar, C. (1990) X-ray diffraction by disordered lamellar structures:
653 Theory and applications to microdivided silicates and carbons. Springer-Verlag, Berlin,
654 371 pp.

655 Drits, V.A., Silvester, E., Gorshkov, A.I., and Manceau, A. (1997) Structure of synthetic
656 monoclinic Na-rich birnessite and hexagonal birnessite: I. Results from X-ray
657 diffraction and selected-area electron diffraction. American Mineralogist, 82, 946-961.

658 Drits, V.A., Lanson, B., Gorshkov, A.I., and Manceau, A. (1998a) Substructure and
659 superstructure of four-layer Ca-exchanged birnessite. American Mineralogist, 83, 97-
660 118.

661 Drits, V.A., Eberl, D.D., and Srodon, J. (1998b) XRD measurement of mean thickness,
662 thickness distribution and strain for illite and illite-smectite crystallites by the Bertaut-
663 Warren-Averbach technique. Clays and Clay Minerals, 46, 38-50.

664 Feng, Q., Yokota, Y., Makita, Y., Yanagisawa, K., and Yamasaki, N. (2001) Synthesis of
665 tunnel manganese oxides from layered manganese oxide by hydrothermal soft
666 chemical process with Rb+ as template. High Pressure Research, 20 (1-6) Special Iss.
667 SI, 33-38.

668 Friedl, G., Wehrli, B., and Manceau, A. (1997) Solid phases in the cycling of manganese
669 in eutrophic lakes: New insights from EXAFS spectroscopy. Geochimica et
670 Cosmochimica Acta, 61, 275-290.

671 Gaillot, A.-C., Flot, D., Drits, V.A., Manceau, A., Burghammer, M., and Lanson, B.

(2003) Structure of K-rich birnessite obtained by high-temperature decomposition of KMnO4. Part 1. Two-layer polytype from 800°C experiments. Chemistry of Materials, 15, 4666-4678.

Gaillot, A.-C., Drits, V.A., Plançon, A., and Lanson, B. (2004) Structure of K-rich birnessite obtained by high-temperature decomposition of KMnO4. Part 2. Phase and structural heterogeneities. Chemistry of Materials, 16, 1890-1905.

Ghiorse, W.C. and Ehrlich, H.L. (1992) Microbial biomineralization of iron and manganese. in H.C.W. Skinner and R.W. Fitzpatrick, Eds., Biomineralization Processes. Iron, Manganeso, Catena supplement 21. pp. 75-99, Cremlingen-Destedt, Germany.

Golden, D.C., Chen, C.C., and Dixon, J.B. (1987) Transformation of birnessite to buserite, todorokite, and manganite under mild hydrothermal treatment. Clays and Clay Minerals, 35, 271-280.

Gorshkov, A.I., Drits, V.A., Putilita, V.S., Pokrovskaya, E.V., and Sivtsov, A.V. (1992) Natural and synthetic birnessites. Lithology and Raw Materials, 6, 67-81 (in Russian).

Harvey, J.W. and Fuller, C.C. (1998) Effect of enhanced manganese oxidation in the hyporheic zone on basin-scale geochemical mass balance. Water Resources Research, 34, 623-636.

Holland, K.L. and Walker, J.R. (1996) Crystal structure modelling of a highly disordered potassium birnessite. Clays and Clay Minerals, 44, 744-748.

Howard, S.A. and Preston, K.D. (1989) Profile fitting of powder diffraction patterns. In D.L. Bish, and J.E. Post, Eds. Modern Powder Diffraction, 20, p. 217-275.

694 Mineralogical Society of America, Washington D.C.

695 Jurgensen, A., Widmeyer, J.R., Gordon, R.A., Bendell-Young, L.I., Moore, M.M., and
696 Crozier, E.D. (2004) The structure of the manganese oxide on the sheath of the
697 bacterium Leptothrix discophora: An XAFS study. American Mineralogist**,** 89**,** 1110-
698 1118.

699 Kay, J.T., Conklin, M.H., Fuller, C.C., and O'Day, P.A. (2001) Processes of nickel and
700 cobalt uptake by a manganese oxide forming sediment in Pinal Creek, Globe Mining
701 District, Arizona. Environmental Science and Technology, 35, 4719-4725.

702 Lanson, B., Drits, V.A., Silvester, E., and Manceau, A. (2000) Structure of H-exchanged
703 hexagonal birnessite and its mechanism of formation from Na-rich monoclinic buserite
704 at low pH. American Mineralogist, 85, 826-838.

705 Lanson, B., Drits, V.A., Feng, Q., and Manceau, A. (2002a) Structure of synthetic Na-
706 birnessite: Evidence for a triclinic one-layer unit cell. American Mineralogist, 87,
707 1662-1671.

708 Lanson, B., Drits, V.A., Gaillot, A.-C., Silvester, E., Plancon, A., and Manceau, A.
709 (2002b) Structure of heavy-metal sorbed birnessite: Part 1. Results from X-ray
710 diffraction. American Mineralogist, 87, 1631-1645.

711 Luo, J. and Suib, S.L. (1997) Preparative parameters, magnesium effects, and anion
712 effects in the crystallization of birnessites. Journal of Physical Chemistry B, 101,
713 10403-10413.

714 Luo, J., Zhang, Q. H., Huang, A. M., Giraldo, O., and Suib, S. L. (1999) Double-aging
715 method for preparation of stabilized Na-buserite and transformations to todorokites

716 incorporated with various metals. Inorganic Chemistry, 38, 6106-6113.

717 Luo, J., Zhang, Q., and Suib, S.L. (2000) Mechanistic and kinetic studies of crystallization
718 of birnessite. Inorganic Chemistry, 39, 741-747.

719 Manceau, A. and Combes, J.M. (1988) Structure of Mn and Fe oxides and oxyhydroxides
720 – a topological approach by EXAFS. Physics and Chemistry of Minerals, 15, 283-295.

721 Manceau, A., Gorshkov, A.I., and Drits, V.A.(1992) Structural Chemistry of Mn, Fe, Co,
722 and Ni in Mn hydrous oxides. II. Information from EXAFS spectroscopy, electron and
723 X-ray diffraction. American Mineralogist, 77, 1144-1157.

724 Manceau, A., Drits, V. A., Silvester, E., Bartoli, C., and Lanson, B. (1997) Structural
725 mechanism of Co(II) oxidation by the phyllomanganate, Na-buserite. American
726 Mineralogist, 82, 1150-1175.

727 Manceau, A., Chateigner, D., and Gates, W.P. (1998) Polarized EXAFS, distance-valence
728 least-squares modeling (DVLS), and quantitative texture analysis approaches to the
729 structural refinement of Garfield nontronite. Physics and chemistry of minerals, 25,
730 347-365.

731 Manceau, A., Lanson, B., Drits, V.A., Chateigner, D., Gates, W.P., Wu, J., Huo, D.F., and
732 Stucki, J.W. (2000a) Oxidation-reduction mechanism of iron in dioctahedral smectites:
733 1. Crystal chemistry of oxidized reference nontronites. American Mineralogist, 85,
734 133-152.

735 Manceau, A., Drits, V.A., Lanson, B., Chateigner, D., Gates, W.P., Wu, J., Hu,o D.F., and
736 Stucki, J.W. (2000b) Oxidation-reduction mechanism of iron in dioctahedral smectites:
737 2. Crystal chemistry of reduced Garfield nontronite. American Mineralogist, 85, 153-

738 172.

739 Manceau, A., Tamura, N., Celestre, R.S., MacDowell, A.A., Geoffroy, N., Sposito G., and
740 Padmore, H.A. (2003) Molecular-scale speciation of Zn and Ni in soil ferromanganese
741 nodules from loess soils of the Mississippi basin. Environmental Science and
742 Technology, 37, 75-80.

743 Manceau, A., Marcus, M. A., Tamura, N., Proux, O., Geoffroy, N., and Lanson, B. (2004)
744 Natural speciation of Zn at the micrometer scale in a clayey soil using X-ray
745 fluorescence, absorption, and diffraction. Geochimica et Cosmochimica Acta, 68,
746 2467-2483.

747 Mandernack, K.W., Fogel, M.L., Tebo, B.M., and Usui, A. (1995a) Oxygen isotope
748 analyses of chemically and microbially produced manganese oxides and manganates.
749 Geochimica et Cosmochimica Acta, 59, 4409-4425.

750 Marble, J.C., Corley, T.L., Conklin, M.H., and Fuller, C.C. (1999) Environmental factors
751 affecting oxidation of manganese in Pinal Creek, Arizona. in D.W. Moranwalp and
752 H.T. Buxton, Eds., Water-Resources Investigation Report, pp. 173-183, US Geological
753 Survey, West Trenton, NJ.

754 McKenzie, R.M. (1971) The synthesis of birnessite, cryptomelane, and some other oxides
755 and hydroxides of manganese. Mineralalogical Magazine, 38, 493-502.

756 McKeown, D.A. and Post, J.E. (2001) Characterization of manganese oxide mineralogy in
757 rock varnish and dendrites using X-ray absorption spectroscopy. American
758 Mineralogist, 86, 701-713.

759 Morgan, J.J. (2000) Manganese in natural waters and earth's crust: Its availability to

760 organisms. in A. Sigel and H. Sigel, Eds., Metal Ions in Biological Systems, Vol. 37,
761 pp. 1-33, Marcel Dekker, New York..

762 Nealson, K.H., Tebo, B.M., and Rosson, R.A. (1988) Occurrence and mechanisms of
763 microbial oxidation of manganese. Advances in Applied Microbiology, 33, 279-318.

764 O'Day, P.A., Rehr, J.J., Zabinsky, S.I., and Brown, G.E. (1994) Extended X-ray
765 absorption fine structure (EXAFS) analysis of disorder and multiple-scattering in
766 complex crystalline solids. Journal of the American Chemical Society, 116, 2938-2949.

767 Pecher, K., McCubbery, D., Kneedler, E., Rothe, J., Bargar, J., Meigs, G., Cox, L.,
768 Nealson, K., and Tonner, B. (2003) Quantitative charge state analysis of manganese
769 biominerals in aqueous suspension using Scanning Transmission X-ray Microscopy
770 (STXM). Geochimica et Cosmochimica Acta 67**,** 1089-1098.

771 Plançon, A. (2002) CALCIPOW- a program for calculating the diffraction by disordered
772 lamellar structures. Journal of Applied Crystallography, 35, 377.

773 Post, J.E. and Veblen, D.R. (1990) Crystal structure determinations of synthetic sodium,
774 magnesium, and potassium birnessite using TEM and the Rietveld method. American
775 Mineralogist, 75, 477-489.

776 Post, J.E., Heaney, P.J., and Hanson, J. (2002) Rietveld refinement of a triclinic structure
777 for synthetic Na-birnessite using synchrotron powder diffraction data. Powder
778 Diffraction, 17, 218-221.

779 Ressler, T (1998) WinXAS: a program for X-ray absorption spectroscopy data analysis
780 under MS-Windows. Journal of Synchrotron Radiation, 5, 118-122.

781 Schlegel, M.L., Manceau, A., Charlet, L., Hazemann, J.L. (2001) Adsorption mechanism

782 of Zn on hectorite as a function of time, pH, and ionic strength. American Journal of
783 Science, 301, 798-830.

784 Shen, Y. F., Zerger, R. P., Deguzman, R. N., Suib, S. L., Mccurdy, L., Potter, D. I., and
785 Oyoung, C. L. (1993) Manganese Oxide Octahedral Molecular Sieves - Preparation,
786 Characterization, and Applications. Science, 260, 511-515.

787 Silvester, E., Manceau, A., and Drits, V.A. (1997) Structure of synthetic monoclinic Na-
788 rich birnessite and hexagonal birnessite: II. Results from chemical studies and EXAFS
789 spectroscopy. American Mineralogist, 82, 962-978.

790 Strobel, P., Charenton, J.C., and Lenglet, M. (1987) Structural chemistry of
791 phyllomanganates: Experimental evidence and structural models. Revue de Chimie
792 Minérale, 24, 199-220.

793 Tebo, B.M. (1991) Manganese(II) oxidation in the suboxic zone of the Black Sea. Deep-
794 Sea Research, 38, S883-S905.

795 Tebo, B.M. and He, L.M. (1999) Microbially mediated oxidative precipitation reactions.
796 in D.L. Sparks and T.J. Grundl, Eds., Mineral-Water Interfacial Reactions Kinetics and
797 Mechanisms, Chapter 20, pp. 393-414, American Chemical Society, Washington, D.C.

798 Tebo, B.M., Ghiorse, W.C., Waasbergen, L.G. van, Siering, P.L., and Caspi, R. (1997)
799 Bacterially mediated mineral formation: Insights into manganese(II) oxidation from
800 molecular genetic and biochemical studies. in J.F. Banfield and K.H. Nealson, Eds.,
801 Reviews in mineralogy, vol. 35, chapter 7, pp. 225-266, Mineralogical Society of
802 America, Washington D.C.

803 Thackeray, M.M., de Kock, A., and David, W.I.F. (1993) Synthesis and structural

804 characterization of defect spinels in the lithium-manganese-oxide system. Materials
805 Research Bulletin, 28, 1041-1049.

806 Tian, Z. R., Yin, Y. G., Suib, S. L., and O'Young, C. L. (1997) Effect of Mg^{2+} ions on the
807 formation of todorokite type manganese oxide octahedral molecular sieves. Chemistry
808 of Materials, 9, 1126-1133

809 Tipping, E., Thompson, D.W., and Davison, W. (1984) Oxidation products of Mn(II) in
810 lake waters. Chemical Geology, 44, 359-383.

811 Toner, B., Fakra, S., Villalobos, M., Warwick, T., and Sposito, G. (2004) Spatially
812 resolved characterization of biogenic manganese oxide production within the biofilm
813 of Pseudomonas putida strain MnB1. Applied and Environmental Microbiology (in
814 press).

815 Viani, A., Gualtieri, A.F., and Artioli, G. (2002) The nature of disorder in montmorillonite
816 by simulation of X-ray diffraction patterns. American Mineralogist, 87, 966-975.

817 Villalobos, M., Toner, B., Bargar, J., and Sposito, G. (2003) Characterization of the Mn
818 oxide produced by *Pseudomonas putida* strain MnB1. Geochimica et Cosmochimica
819 Acta, 67, 2649-2662.

820 Wadsley, A.D. (1955) The crystal structure of chalcophanite, $ZnMn_3O_7.3H_2O$, Acta
821 Crystallographica, 8, 1165-1172.

822 Wehrli, B., Friedl, G., and Manceau, A. (1995) Reaction rates and products of manganese
823 oxidation at the sediment-water interface. in Aquatic Chemistry. In C.P. Huang,
824 C.O'Melia and J.J. Morgan, Eds., Advances in Chemistry Series 244, p. 111-134,
825 American Chemical Society, Washington D.C.

826 Zabinsky, S.I., Rehr, J.J., Ankudinov, A., Albers, R.C., and Eller, M.J. (1995) Multiple
827 scattering calculations of X-ray absorption spectra, Physical Reviews, 52, 2995-3009.
828
829
830
831
832 **FIGURES**
833
834 **Fig. 1.** Experimental XRD patterns of the Mn oxide samples. (a) acid birnessite, (b) δ-
835 MnO_2, (c) biogenic oxide with cell material, (d) cell material without the biogenic oxide.
836
837 **Fig. 2.** Comparison between experimental ('+' symbols) and calculated (solid line) XRD
838 patterns for the various Mn oxide samples. Structural parameters used for calculations are
839 listed in Tables 2 and 3. Calculations are limited to the 00*l* reflections occurring below 35˚2θ
840 CuKα. (a) acid birnessite, (b) δ-MnO_2, (c) biogenic oxide with cell material. The lower gray
841 trace in (c) is the experimental XRD pattern for cell material without the biogenic oxide.
842
843 **Fig. 3.** Comparison between experimental and calculated XRD patterns for the various Mn
844 oxide samples. Patterns as for Figure 2. Structural parameters used for calculations are listed
845 in Tables 2 and 3. Calculations are performed for the 20,11 and for the 02,31 bands (maxima
846 at ~37 and 66°2θ CuKα, respectively). (a) δ-MnO_2, (b) acid birnessite, (c) biogenic oxide.
847
848 **Fig. 4.** Structure model for the various Mn oxide samples. (a) Projection on the **ab** plane.
849 The upper surface of the layer is shown as light shaded triangles. O_{layer} atoms of this upper
850 surface are shown as solid circles, whereas Mn_{layer} atoms are not shown. Large open circles

represent Na^+ cations and H_2O molecules in δ-MnO_2 [(0.225,0,0.5) – Position O3]. K represents the position of interlayer K^+ cations in the acid birnessite sample. Positions labeled Alt.n (n = 1, 2, 3) represent test positions to assess the sensitivity of calculated XRD patterns to the position of interlayer species. The dashed triangle outlines the upper surface of the $Mn_{interlayer}$ coordination octahedron which is defined by three $H_2O_{interlayer}$ (small open circles). (b) Projection along the **b** axis. Open and solid symbols indicate atoms at $y = 0$ and $y = \pm½$, respectively. Large circles represent O_{layer} atoms, small circles represent Mn atoms. The solid squares represents a vacant layer site. The dashed line outlines the $Mn_{interlayer}$ coordination octahedron which is defined by O_{layer} and $H_2O_{interlayer}$.

Fig. 5. Comparison between experimental and calculated XRD patterns for δ-MnO_2. Patterns as for Figure 2. Structural parameters used for calculations are listed in Tables 2 and 3a. Calculations are performed for the 20*l*,11*l* and for the 02*l*,31*l* sets of reflections (maxima at ~37 and 66°2θ CuKα, respectively). (a) Interlayer Na^+ cations and H_2O molecules are located above or below layer octahedra [position (0.0, 0.0, 0.5) – Alt. 1 in Fig. 4] rather than in the optimum O3 position (0.225, 0.0, 0.5) (Fig. 3a). (b) Interlayer Na^+ cations and H_2O molecules are located in (0.333, 0.0, 0.5) (position Alt. 2 in Fig. 4) rather than in the optimum O3 position (0.225, 0.0, 0.5). (c) Interlayer Na^+ cations and H_2O molecules are located above/below the tridentate cavities at the layer surface [Position "Alt. 3" in Fig. 4 with coordinates (-0.167, 0.0, 0.5)] rather than in the optimum O3 position (0.225, 0.0, 0.5).

Fig. 6. Comparison between experimental and calculated XRD patterns for δ-MnO_2. Patterns as for Figure 2. Structural parameters used for calculations are listed in Tables 2 and 3a. Calculations are performed for the 20*l*,11*l* and for the 02*l*,31*l* sets of reflections (maxima at ~37 and 66°2θ CuKα, respectively). (a) Mean radial dimension of the CSD in the **ab** plane

876 is increased from the optimum 5.8 nm (Fig. 3a) to 10.0 nm. (b) Mean radial dimension of the
877 CSD in the **ab** plane is decreased from the optimum 5.8 nm to 3.0 nm.
878
879 **Fig. 7.** Comparison between experimental and calculated XRD patterns for the biogenic
880 oxide. Patterns as for Figure 2. Structural parameters used for calculations are listed in
881 Tables 2 and 3c. Calculations are performed for the 20*l*,11*l* an for the 02*l*,31*l* sets of
882 reflections (maxima at ~37 and 66°2θ CuKα, respectively). (a) Amounts of vacant layer sites
883 and of interlayer Mn cations are assumed to be 0.167 and 0.100, as compared to the optimum
884 0.167 and 0.167 values (Fig. 3c), respectively. (b) Amounts of vacant layer sites and of
885 interlayer Mn cations are assumed to be 0.100 and 0.100, as compared to the optimum 0.167
886 and 0.167 values, respectively. (c) Interlayer Mn cations are located above/below the
887 tridentate cavities at the layer surface [Position "Alt. 3" in Fig. 4 with coordinates (-0.167,
888 0.0, 0.299)] rather than in the optimum position (0.0, 0.0, 0.299).
889
890 **Fig. 8.** (a) k^3-weighted Mn K-edge EXAFS spectra of Mn oxides lacking 3D ordering and of
891 H-birnessite. (b) Magnitude of the Fourier transform (uncorrected for phase shifts).
892
893 **Fig. 9.** Comparison between k^3-weighted Mn K-edge EXAFS spectra of (a) the cleaned
894 biogenic Mn oxide and δ-MnO_2, (b) the cleaned biogenic Mn oxide and acid birnessite, and
895 (c) the uncleaned biogenic Mn oxide and H-birnessite. The arrow denotes the area where the
896 biogenic oxide and H-birnessite overlap (Manceau et al. 1997).
897
898 **Fig. 10.** Comparison between the magnitude and imaginary part of the Fourier transforms
899 (uncorrected for phase shifts) for (a) the cleaned biogenic Mn oxide and δ-MnO_2, (b) the
900 cleaned biogenic Mn oxide and acid birnessite, and (c) the uncleaned biogenic Mn oxide and

H-birnessite. The letters refer to the four different shells identified. A indicates the peak due to Mn-O(1) distance, B to the Mn-Mn(1) distance, C mostly to the Mn-Mn(tc) distance, and D to the third Mn layer shell distance. The latter was not modeled with the single scattering model employed in the spectral simulations. The arrow denotes the area where the biogenic oxide and H-birnessite overlap (Manceau et al. 1997).

Fig. 11. Fourier-filtered experimental EXAFS spectra and FEFF simulations of the $1.0 < R+\Delta R < 3.1$ Å region for (a) δ-MnO_2, (b) acid birnessite, (c) NaOCl-cleaned biogenic Mn oxide, according to the parameters listed in Table 5.

Fig. 12. Idealized hexagonal layer structure of edge-sharing Mn^{4+}-O_6 octahedra (inset at left) for δ-MnO_2.

Fig. 13. Comparison between the EXAFS data of the cleaned and uncleaned biogenic Mn oxide. (a) k^3-weighted Mn K-edge EXAFS spectra. (b) Magnitude and imaginary part of the Fourier transforms (uncorrected for phase shifts).

Fig. 14. Fourier-filtered experimental EXAFS spectra of the $1.0 < R+\Delta R < 3.1$ Å region for (a) H-birnessite and the uncleaned biogenic Mn oxide; and FEFF simulations for (b) H-birnessite, and (c) the uncleaned biogenic Mn oxide, according to the parameters listed in Table 5.

Fig. 15. EXAFS contribution of the Mn-O(1) shell for a theoretical Mn oxide composed of 80 % Mn^{4+} and 20 % Mn^{2+}, which shows that despite the widely differing $\chi(k)$ frequencies (a)

925 obtained, and corresponding radial structure functions (b), the dominant $\chi(k)$ function and

926 RSF of the mixture is that of the shorter Mn^{4+}-O distance, with amplitude reductions.

927

927

928 **Table 1.** Physicochemical properties of the Mn oxides investigated
929

Mn oxide	H_2O content (% w/w) (± 0.02)	Average Mn Oxidation Number (± 0.02) †	Structural Alc*/Mn_{tot} (mol %)†
Biogenic#	10.0	3.90 ±0.05	(pH 8.1) 16.7 ±0.3
Acid Birnessite	7.5	3.96	(pH 5.6) 20.4 ±0.8
δ-MnO_2	15.8	4.02	(pH 8.1) 25.3 ±0.1

Note: †From Villalobos et al. (2003); *Alc refers to the alkaline counterion, which is K^+ for "acid birnessite" and Na^+ for the others; #From *Pseudomonas putida*.

930
931
932
933

933 **Table 2.** Optimum structural parameters used for the simulation of the three experimental X-
934 ray diffraction profiles (cf. Figs. 2, 3).
935

Atom	δ-MnO_2	Acid birnessite	Biogenic oxide
a (Å)	4.916	4.916	4.916
b (Å)	2.838	2.838	2.838
d(001) (Å)	7.20	7.20	7.20
Average CSD size (along the **c*** axis)	2.6	5.8	2.8
Average CSD size (in the **ab** plane)	60	70	85

Note: Optimal values were determined by trial-and-error fitting of the experimental XRD patterns. *a* and *b* parameters were determined from the simulation of the *hkl* bands whereas the *c* parameter was estimated from the simulation of the 00l reflections. Coherent scattering domain (CSD) sizes along **c*** are expressed as number of layers, whereas the average radius of the CSDs in the **ab** plane is expressed in Å. The latter values have been determined to fit the 20,11 band.

936
937

937 **Table 3a.** Optimum structural parameters used for the simulation of δ-MnO_2 X-ray

938 diffraction profile (cf. Fig. 3a).

939

Atom	*x*	*y*	*ζ*	Occ.	*x*	*y*	*ζ*	Occ.
Mn_{layer}	0	0	0	0.94	-	-	-	-
O_{layer}	0.333	0	1.00	1.00	-0.333	0	-1.00	1.00
$Mn_{interlayer}$	-	-	-	0.00	-	-	-	0.00
$H_2O_{interlayer}$	-	-	-	0.00	-	-	-	0.00
$Na_{interlayer}$	0.225	0	3.60	0.04	-0.225	0	-3.60	0.04
$Na_{interlayer}$	-0.1125	0.3375	3.60	0.04	-0.1125	-0.3375	3.60	0.04
$Na_{interlayer}$	0.1125	0.3375	-3.60	0.04	0.1125	-0.3375	-3.60	0.04
$H_2O_{interlayer}$	0.225	0	3.60	0.12	-0.225	0	-3.60	0.12
$H_2O_{interlayer}$	-0.1125	0.3375	3.60	0.12	-0.1125	-0.3375	3.60	0.12
$H_2O_{interlayer}$	0.1125	0.3375	-3.60	0.12	0.1125	-0.3375	-3.60	0.12

Note: Optimal values were determined by trial-and-error fitting of the experimental XRD patterns. *x*, and *y* coordinates are expressed as fractions of the *a* and *b* parameters, respectively. Coordinates along the **c*** axis, *ζ*, are expressed in Å to emphasize the thickness of layer and interlayer polyhedra. Un-refined thermal *B* factors are 0.5 for Mn_{layer}, 1.0 for O_{layer} and $Mn_{interlayer}$, and 1.5 for interlayer H_2O molecules associated with $Mn_{interlayer}$, and 2.0 for other interlayer species (alkali cations and H_2O molecules)

940

941

941 **Table 3b.** Optimum structural parameters used for the simulation of acid birnessite X-ray

942 diffraction profile (cf. Fig. 3b).

943

Atom	*x*	*y*	*ζ*	Occ.	*x*	*y*	*ζ*	Occ.
Mn_{layer}	0	0	0	0.88	-	-	-	-
O_{layer}	0.333	0	1.00	1.00	-0.333	0	-1.00	1.00
$Mn_{interlayer}$	0	0	2.15	0.04	0	0	-2.15	0.04
$H_2O_{inter.}$	-0.333	0	3.35	0.12	0.333	0	-3.35	0.12
$K_{interlayer}$	-0.203	0	3.60	0.03	0.203	0	-3.60	0.03
$K_{interlayer}$	-0.4167	0.125	3.60	0.03	-0.4167	-0.125	3.60	0.03
$K_{interlayer}$	0.4167	0.125	-3.60	0.03	0.4167	-0.125	-3.60	0.03
$H_2O_{inter.}$	0.200	0	3.60	0.09	-0.200	0	-3.60	0.09
$H_2O_{inter.}$	-0.100	0.300	3.60	0.09	-0.100	-0.300	3.60	0.09
$H_2O_{inter.}$	0.100	0.300	-3.60	0.09	0.100	-0.300	-3.60	0.09

944

945

945 **Table 3c.** Optimum structural parameters used for the simulation of the biogenic oxide X-ray

946 diffraction profile (cf. Fig. 3c).

947

Atom	*x*	*y*	*ζ*	Occ.	*x*	*y*	*ζ*	Occ.
Mn_{layer}	0	0	0	0.833	-	-	-	-
O_{layer}	0.333	0	1.00	1.00	-0.333	0	-1.00	1.00
$Mn_{interlayer}$	0	0	2.15	0.0833	0	0	-2.15	0.0833
$H_2O_{inter.}$	-0.333	0	3.35	0.25	0.333	0	-3.35	0.25
$Na_{interlayer}$	0.225	0	3.60	0.04	-0.225	0	-3.60	0.04
$Na_{interlayer}$	-0.1125	0.3375	3.60	0.04	-0.1125	-0.3375	3.60	0.04
$Na_{interlayer}$	0.1125	0.3375	-3.60	0.04	0.1125	-0.3375	-3.60	0.04
$H_2O_{inter.}$	0.225	0	3.60	0.12	-0.225	0	-3.60	0.12
$H_2O_{inter.}$	-0.1125	0.3375	3.60	0.12	-0.1125	-0.3375	3.60	0.12
$H_2O_{inter.}$	0.1125	0.3375	-3.60	0.12	0.1125	-0.3375	-3.60	0.12

948

949

949 **Table 4.** Typical inter-atomic distances calculated from the optimum atomic coordinates.

950

Atomic pair	δ-MnO_2	Acid birnessite	Biogenic oxide
Mn_{layer}-O_{layer}	1.920 Å	1.920 Å	1.920 Å
$Mn_{inter.}$-O_{layer}	-	2.00 Å	2.00 Å
$Mn_{inter.}$-H_2O	-	2.03 Å	2.03 Å
*$Alc_{inter.}$-O_{layer}	2.65 Å	2.97 Å	2.65 Å
*Alc_{inter}-H_2O	2.838 Å	2.93 x1 / 2.99 x2 / 3.02x2 Å	2.838 Å
H_2O_{inter}-O_{layer}	2.65 Å	2.68 Å	2.65 Å

951

952 * Alc_{inter} refers to the alkaline interlayer counterion, which is K^+ for "acid birnessite" and Na^+
953 for the others. Inter-atomic distances from interlayer species to O_{layer} are calculated with
954 respect to a unique layer, without adjacent layer whose actual position is unknown as a result
955 of the turbostratic stacking.
956

Table 5. Optimized simulation parameters of K-edge Mn EXAFS for biogenic Mn oxide and synthetic analogs.

Sample	Shells†												
	Mn-O (1)			Mn-O (2)‡			Mn-Mn (1)			Mn-Mn (tc)			ΔE
	R(Å)	N	σ^2 ($Å^2$)	R(Å)	N	σ^2 ($Å^2$)	R(Å)	N	σ^2 ($Å^2$)	R(Å)	N	σ^2 ($Å^2$)	
δ-MnO_2	1.90	5.7	0.0042	3.49	6*	0.0167	2.88	4.3	0.0042	-	-	-	0.6
Acid Birnessite	1.90	5.3	0.0038	3.50	6*	0.0134	2.88	4.6	0.0045	-	-	-	0.8
H-birnessite	1.91	4.5	0.0032	3.61	6*	0.0049	2.89	4.8	0.0051#	3.49	2.8	0.0051#	1.6
Biogenic (clean)	1.90	5.1	0.0035	3.42	6*	0.0149	2.87	2.9	0.0033	-	-	-	-0.4
Biogenic (unclean)	1.91	4.8	0.0030	3.61	6*	0.0049	2.87	4.8	0.0051#	3.49	2.8	0.0051#	3.6
λ-MnO_2 (standard)	1.91	6.0	0.0025	3.52	6*	0.0088	2.85	6.0	0.0028				1.5

Note: †S_0^2 values used for the amplitude normalization were 0.73 for the O(1) shell and 0.80 for the Mn shells. Typical uncertainty on Mn-O (1), Mn-Mn (1), and Mn-Mn (tc) interatomic distances and coordination numbers are 0.02 Å and ± 1.5, respectively.

‡ The Mn-O(2) shell contribution is very weak and thus a high correlation occurs between the optimized frequency and ΔE, resulting in a low precision of the predicted parameters.

*Fixed value in the optimization procedure.

#σ values for the Mn(1) and Mn(tc) shells were floated but kept identical.

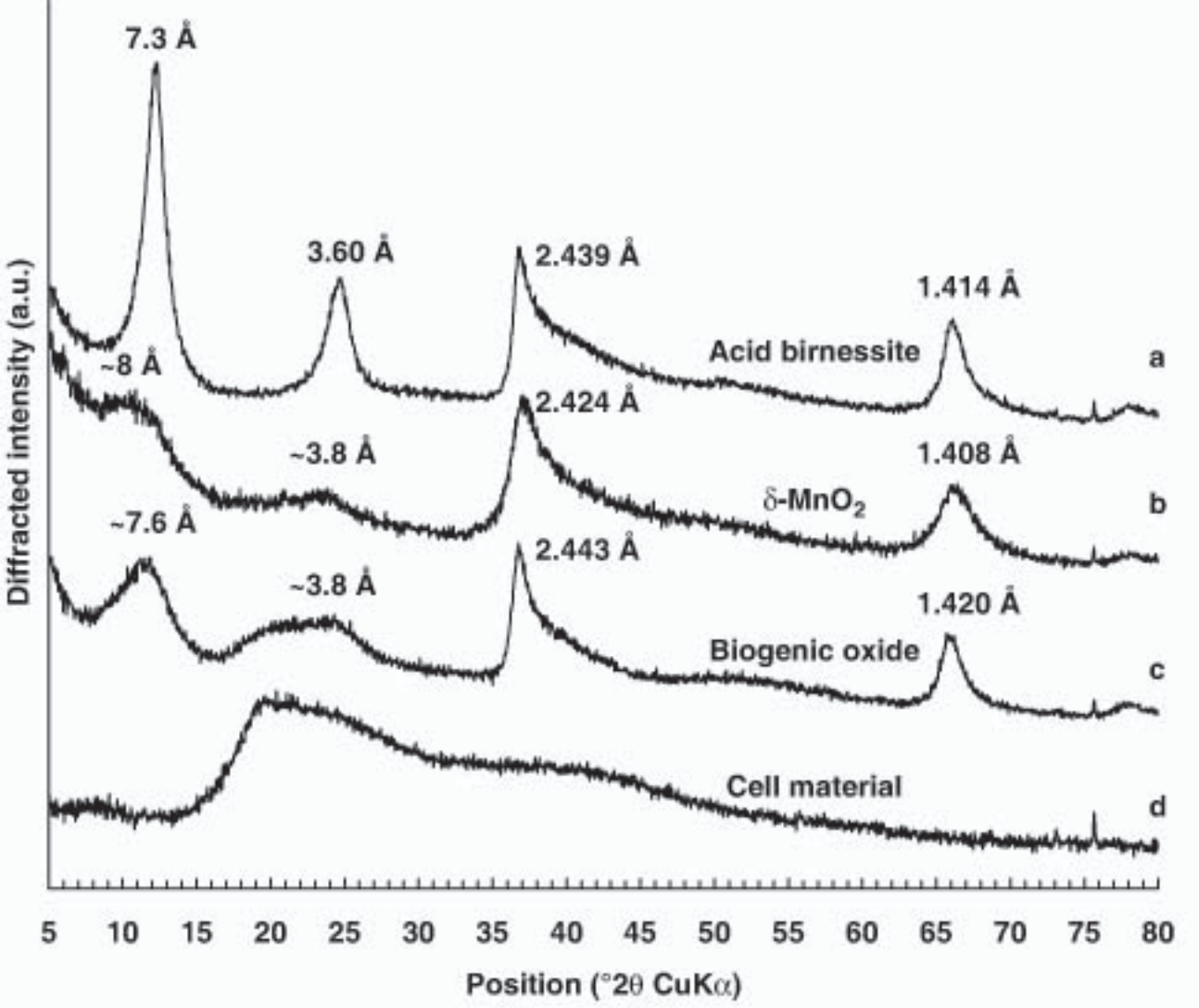

Villalobos et al., Fig_01

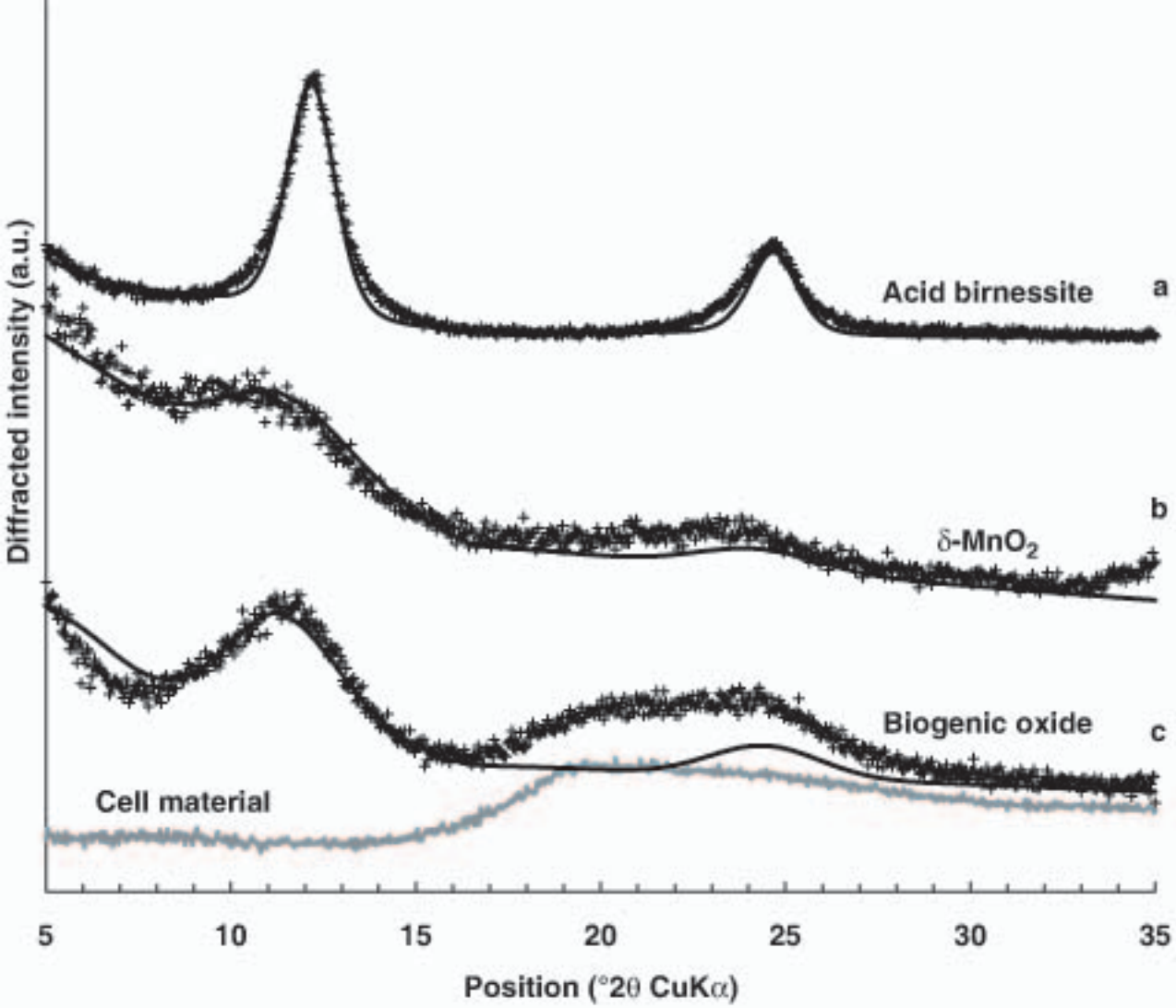

Villalobos et al., Fig_02

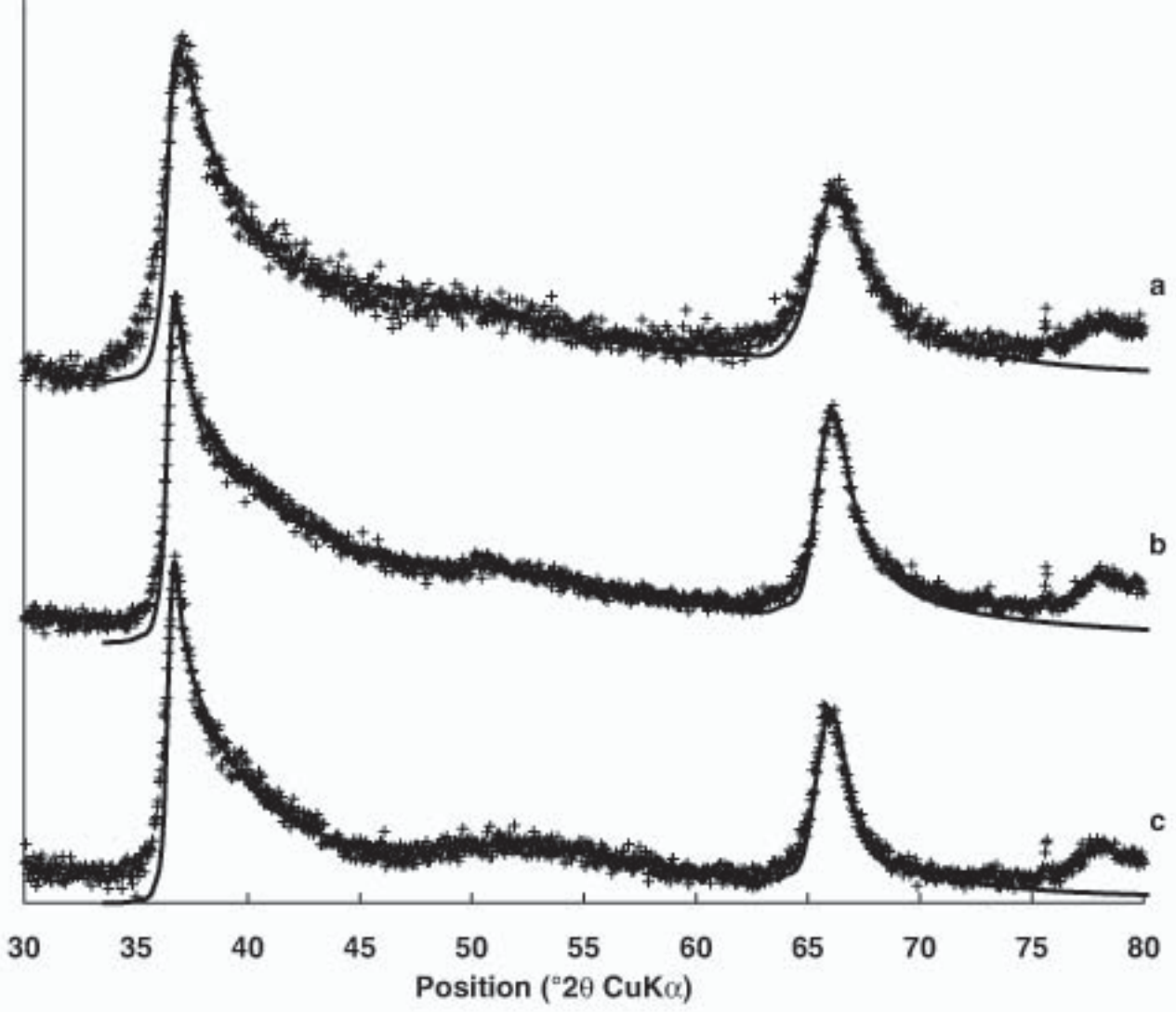

Villalobos et al., Fig_03

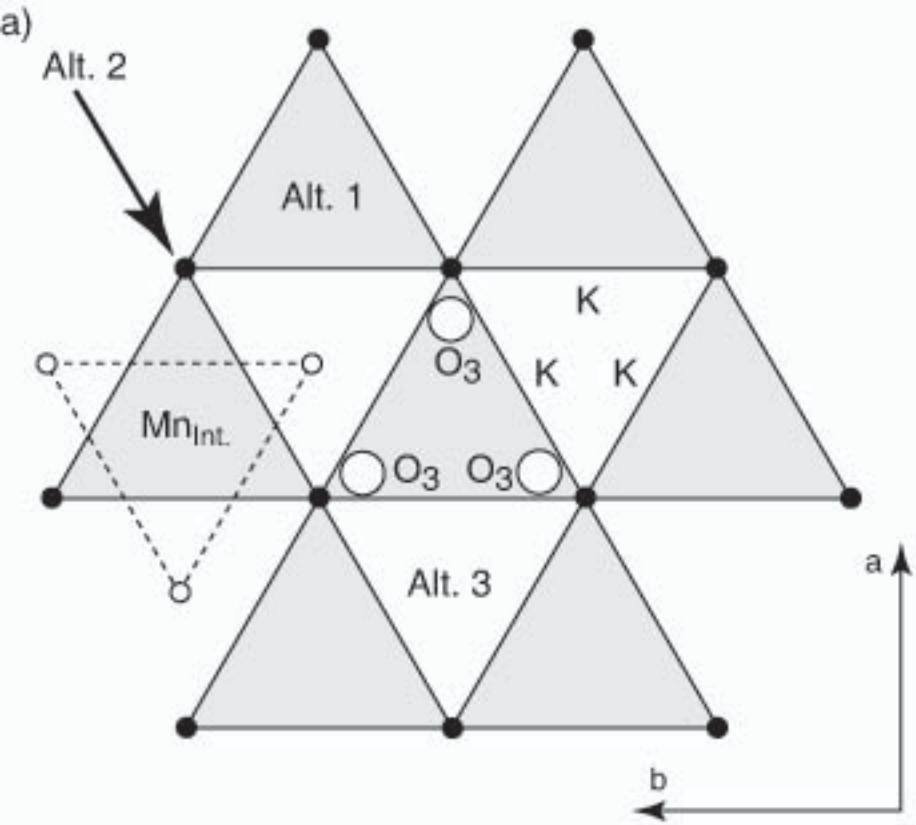

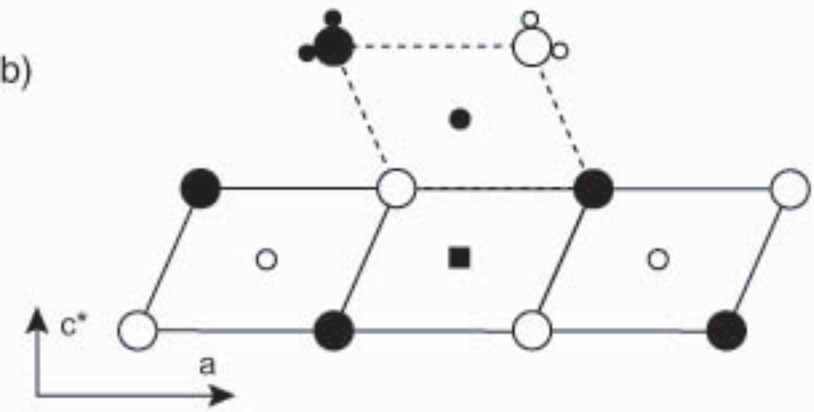

Villalobos et al., Fig_04

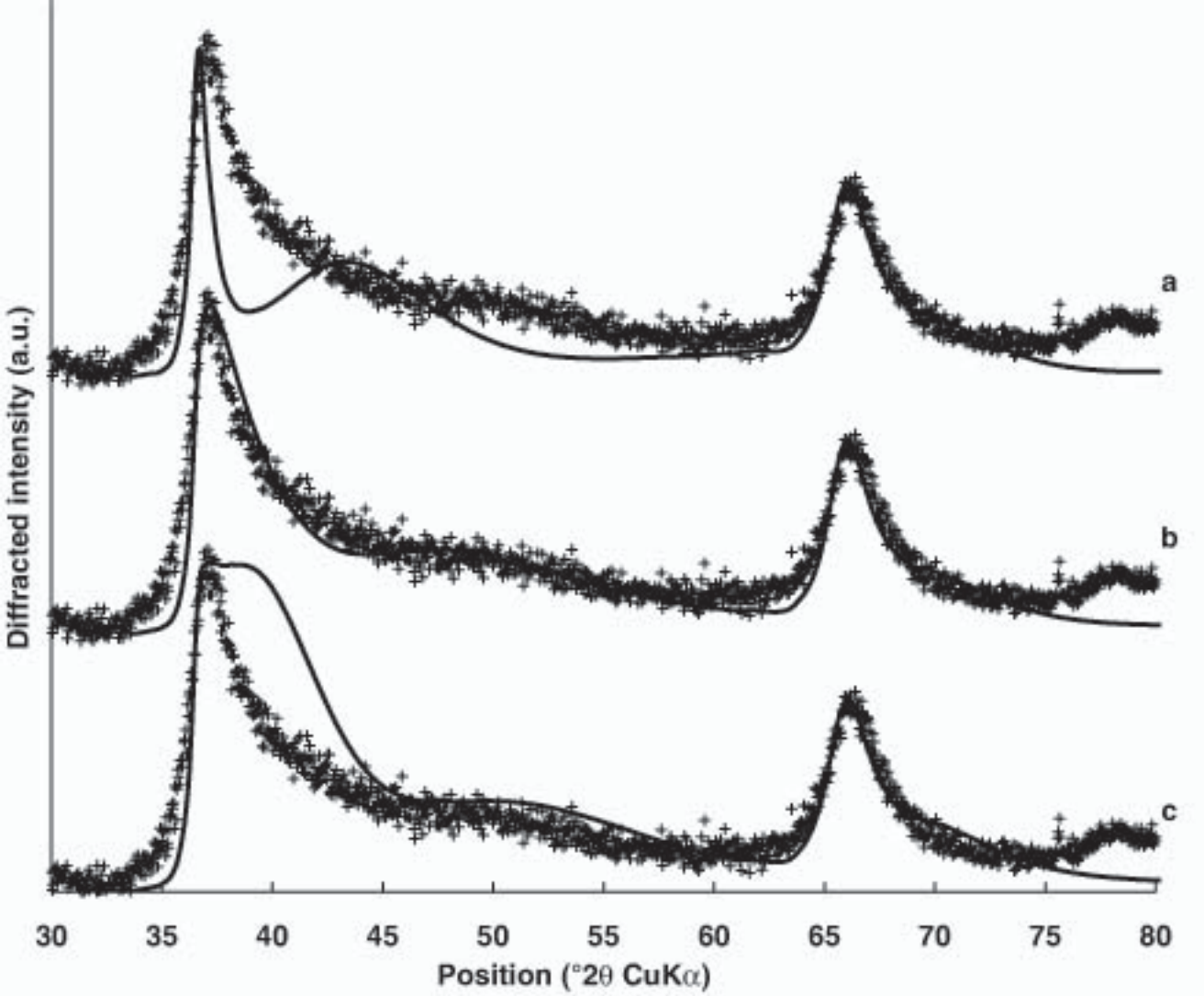

Villalobos et al., Fig_05

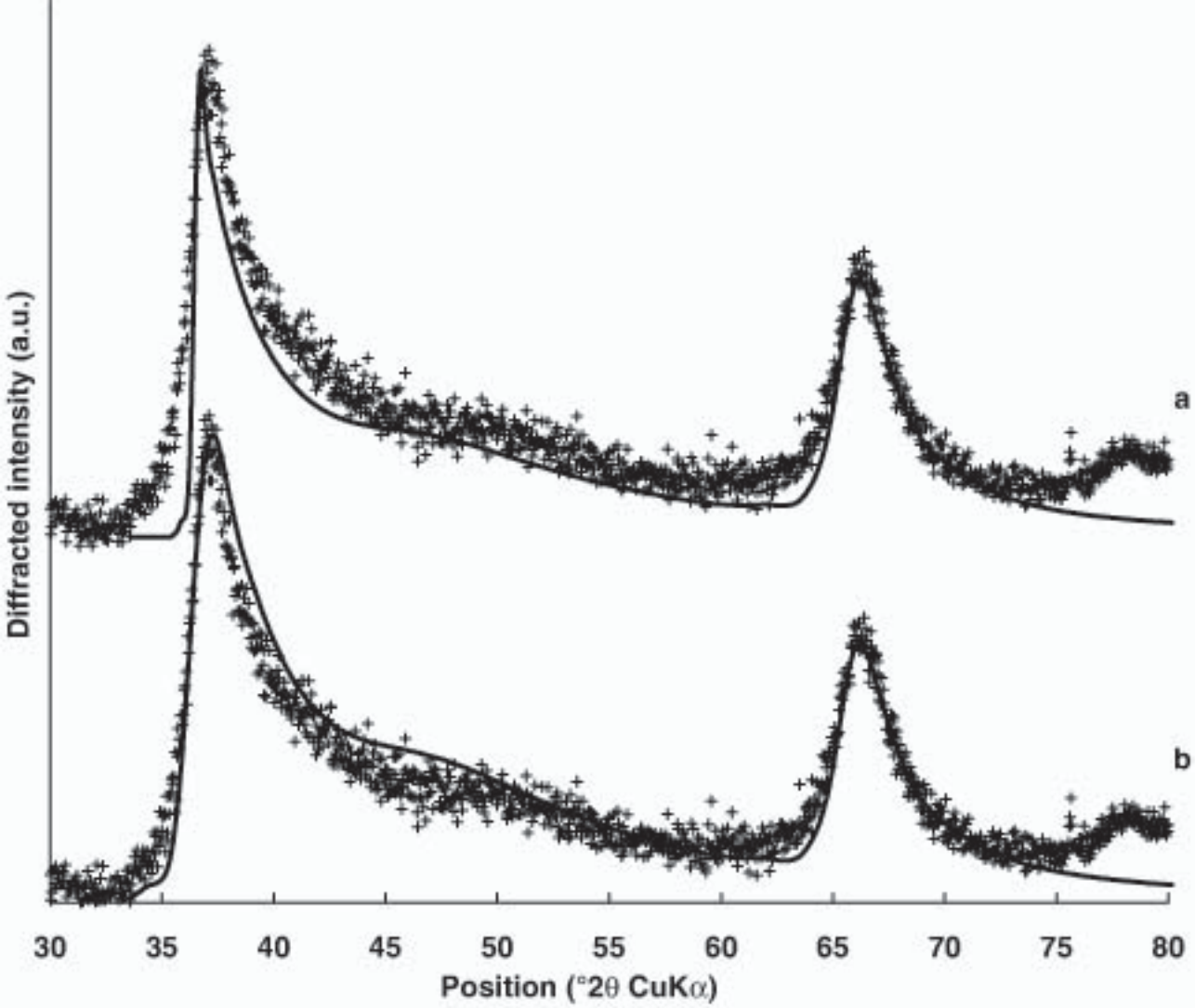

Villalobos et al., Fig_06

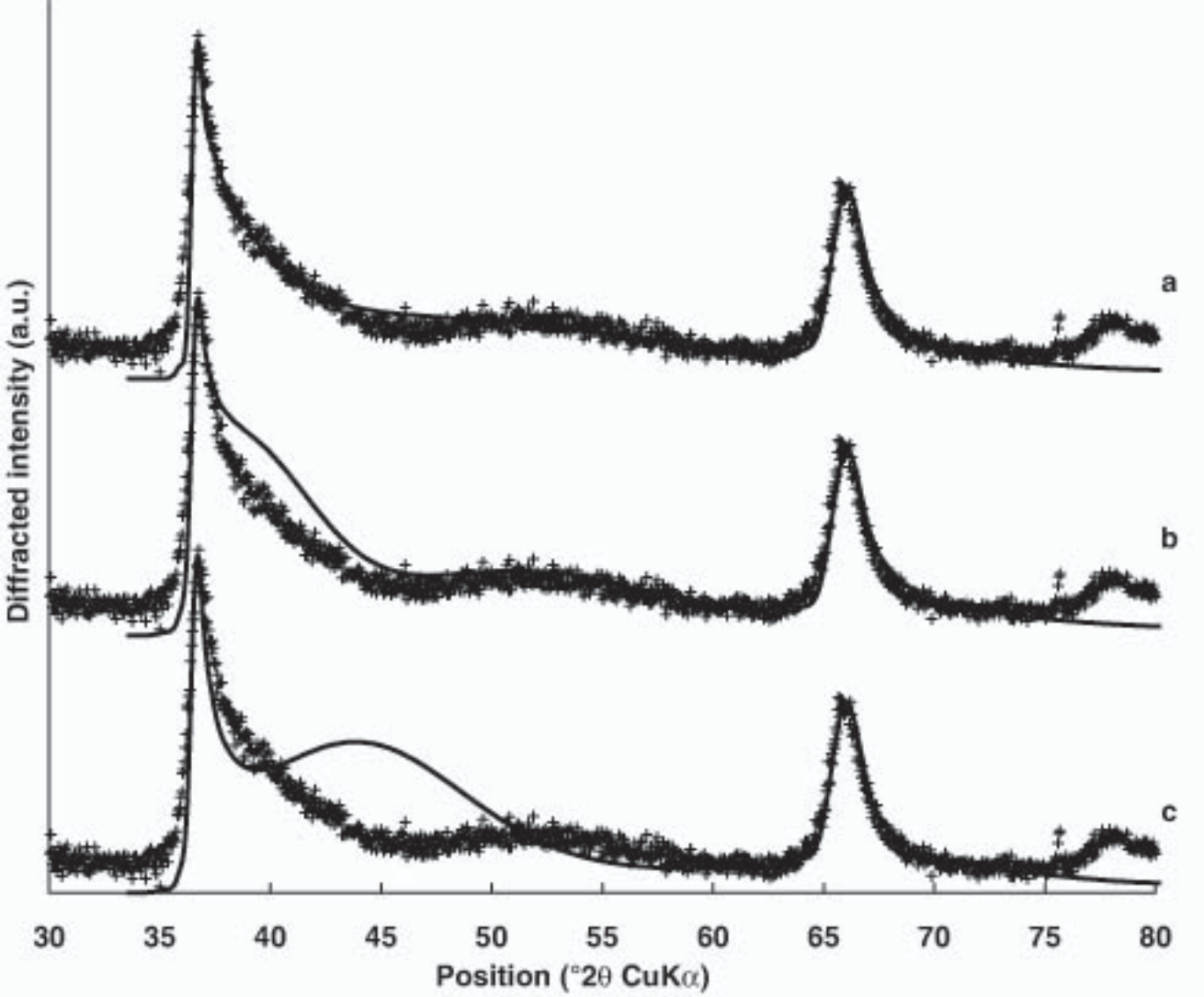

Villalobos et al., Fig_07

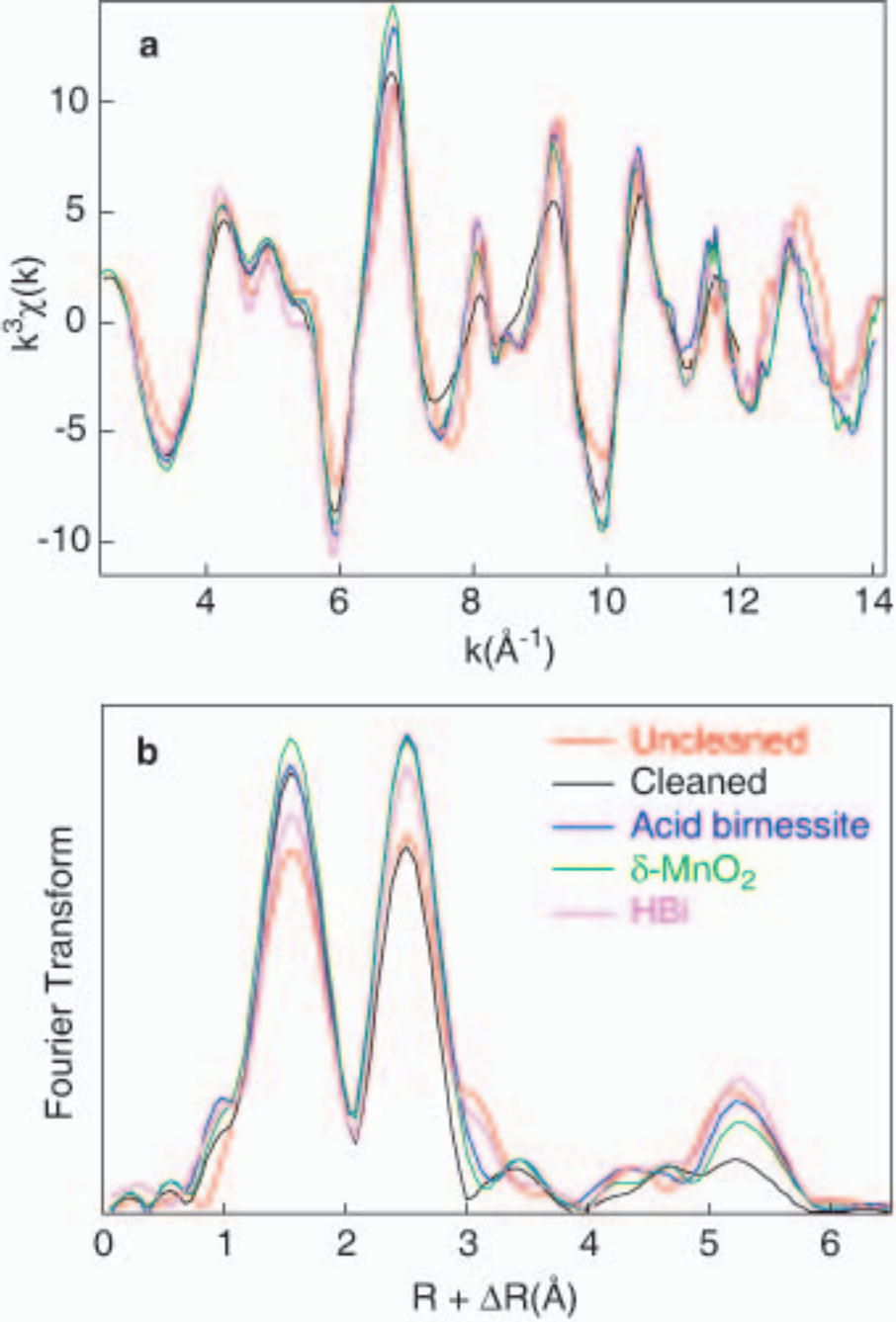

Villalobos et al., Fig_08

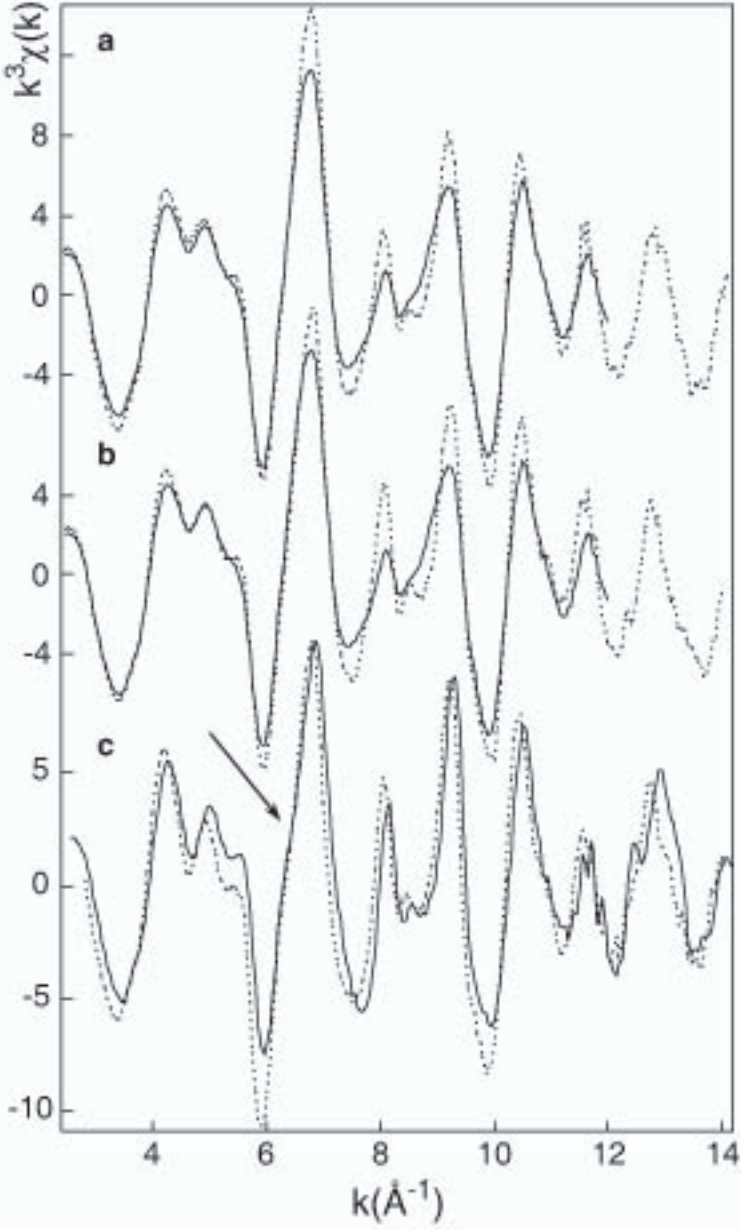

Villalobos et al., Fig_09

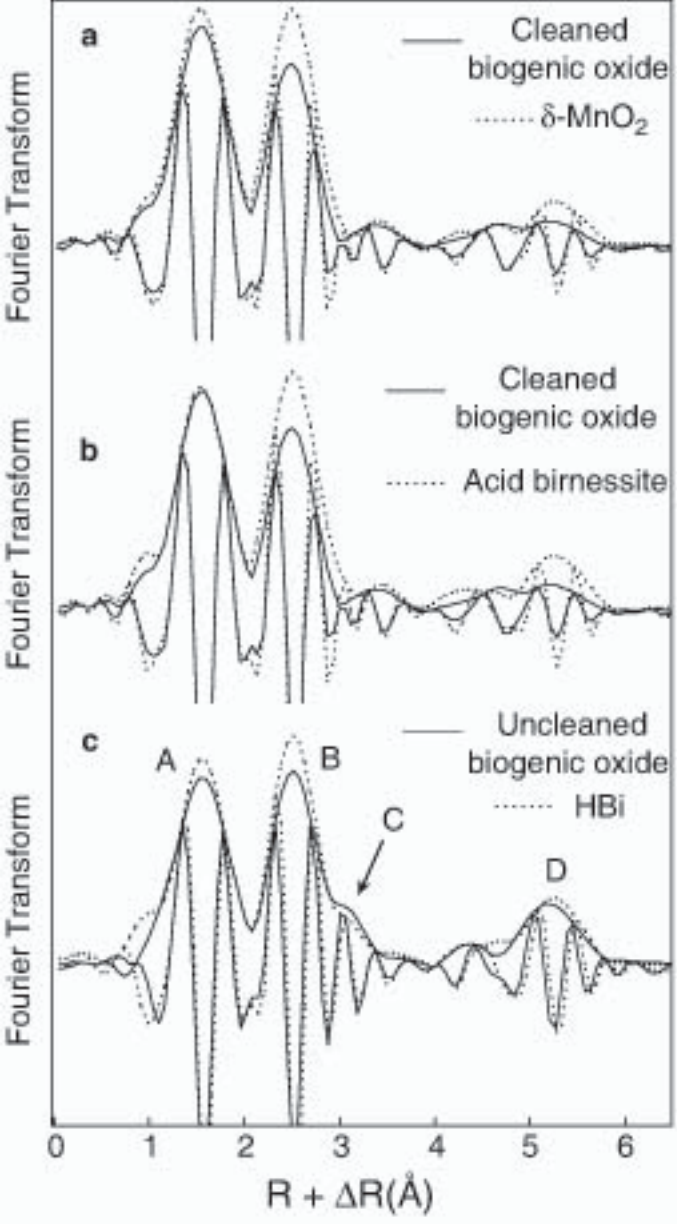

Villalobos et al., Fig_10

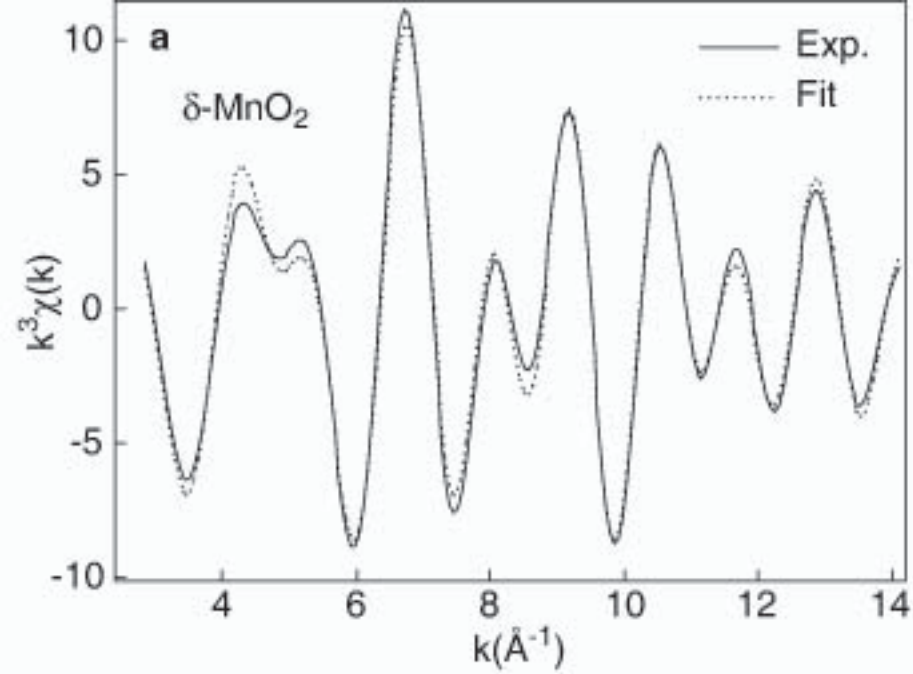

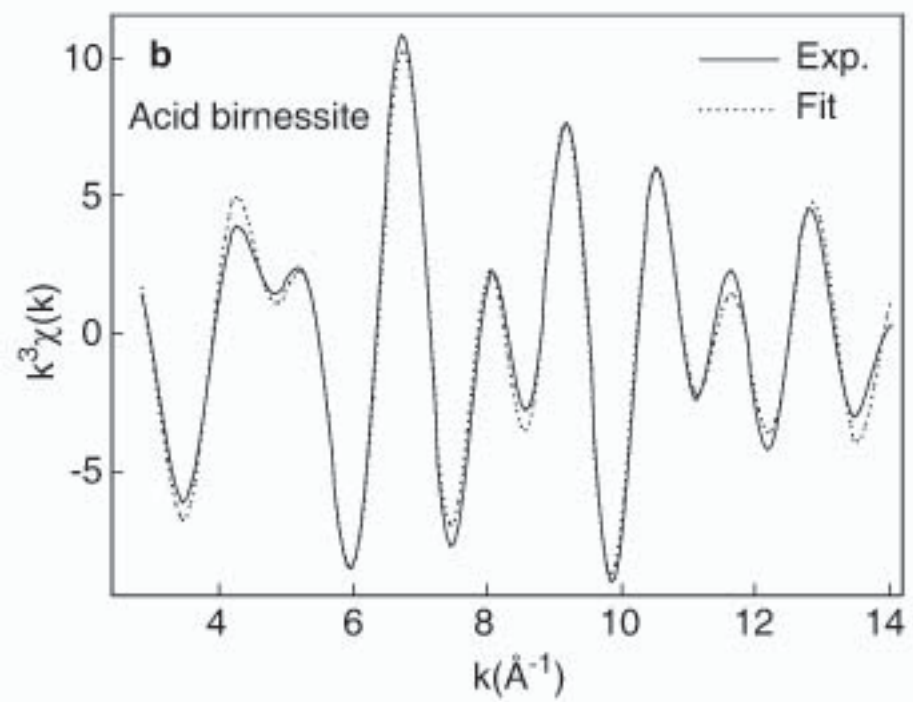

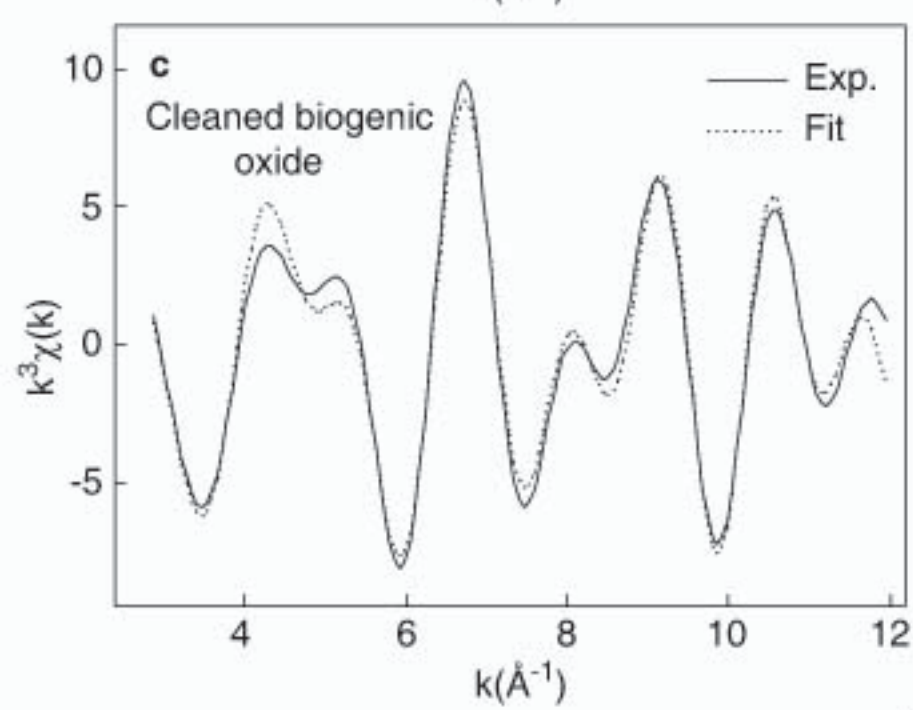

Villalobos et al., Fig_11

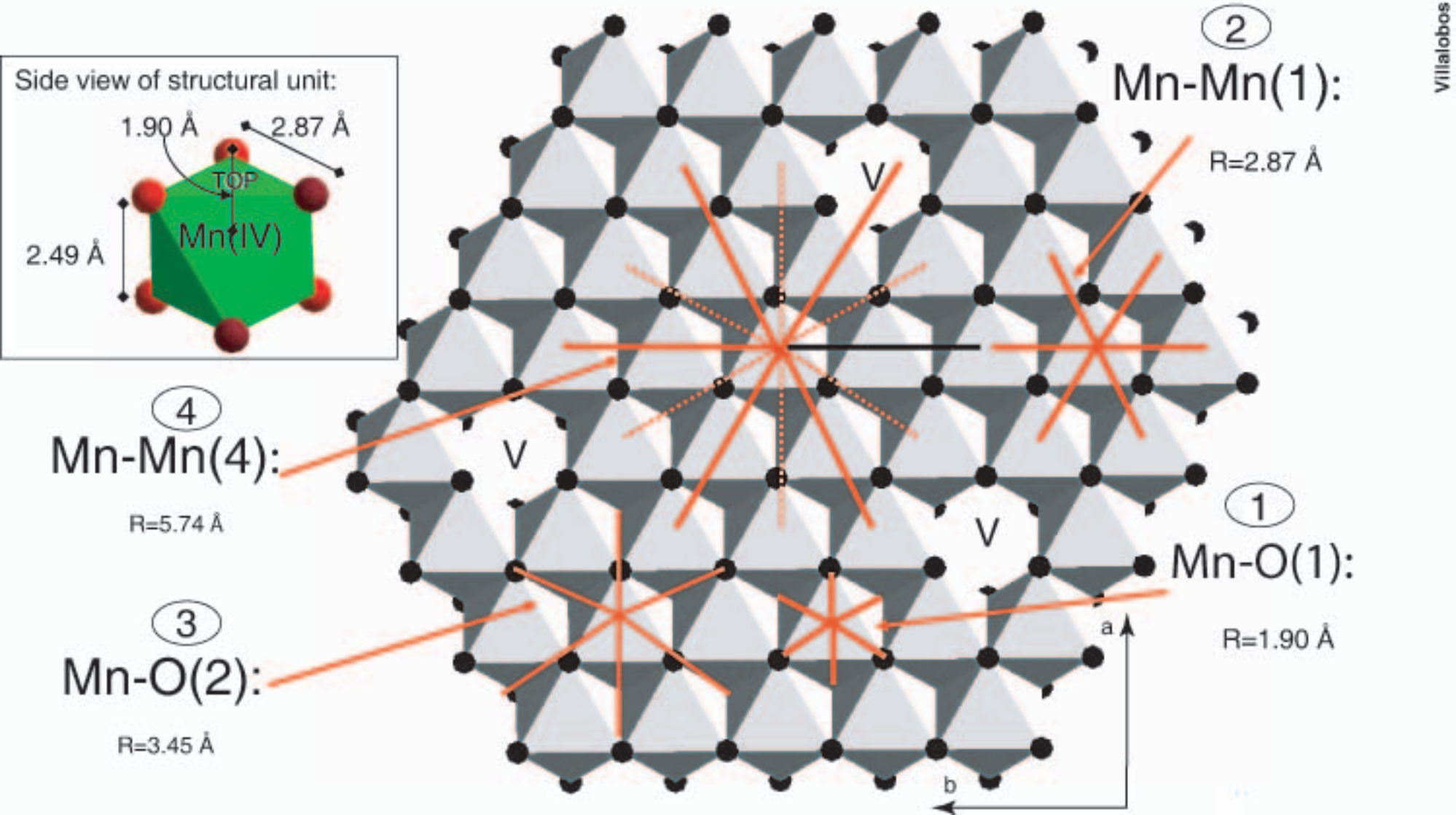

Villalobos et al., Fig_12

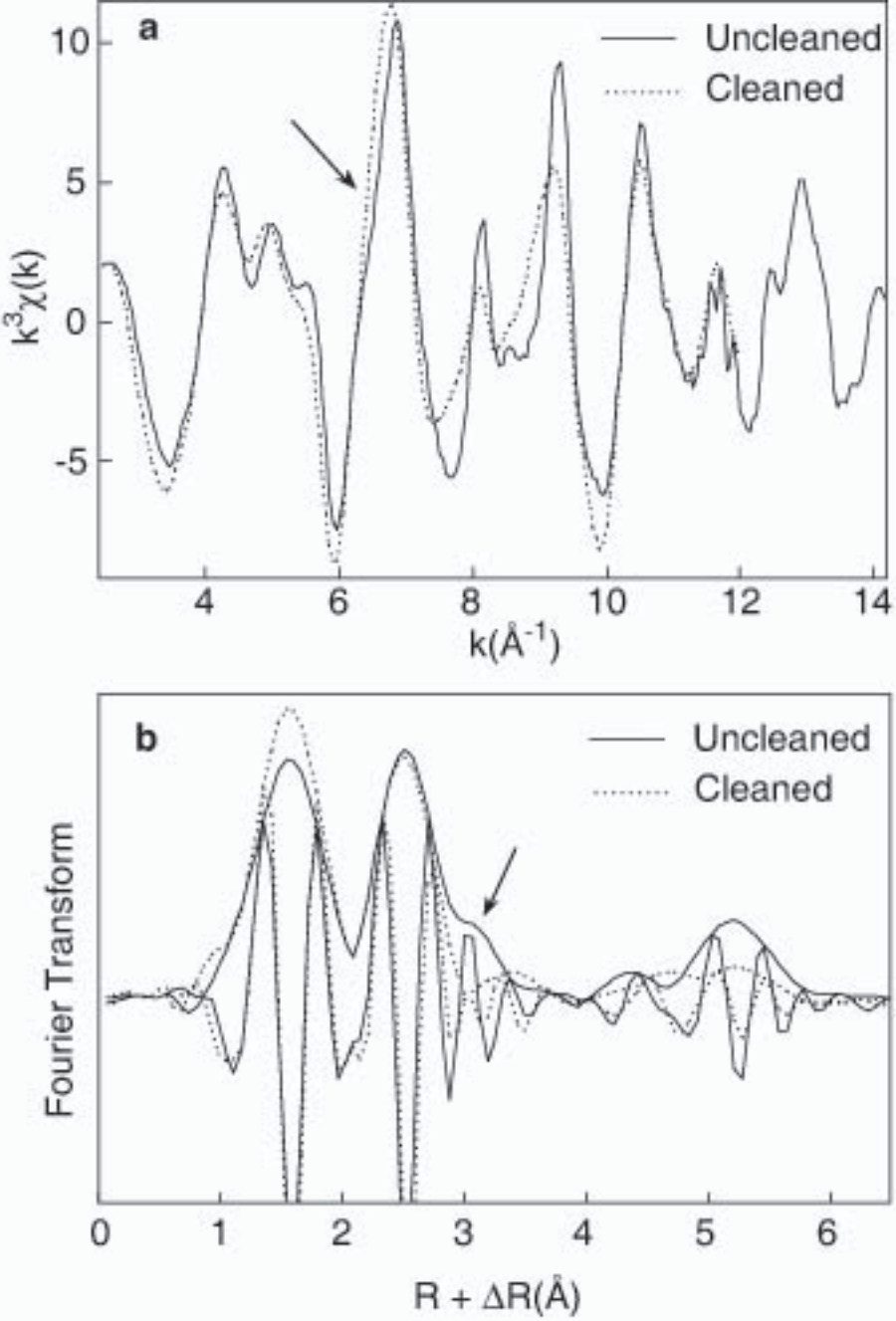

Villalobos et al., Fig_13

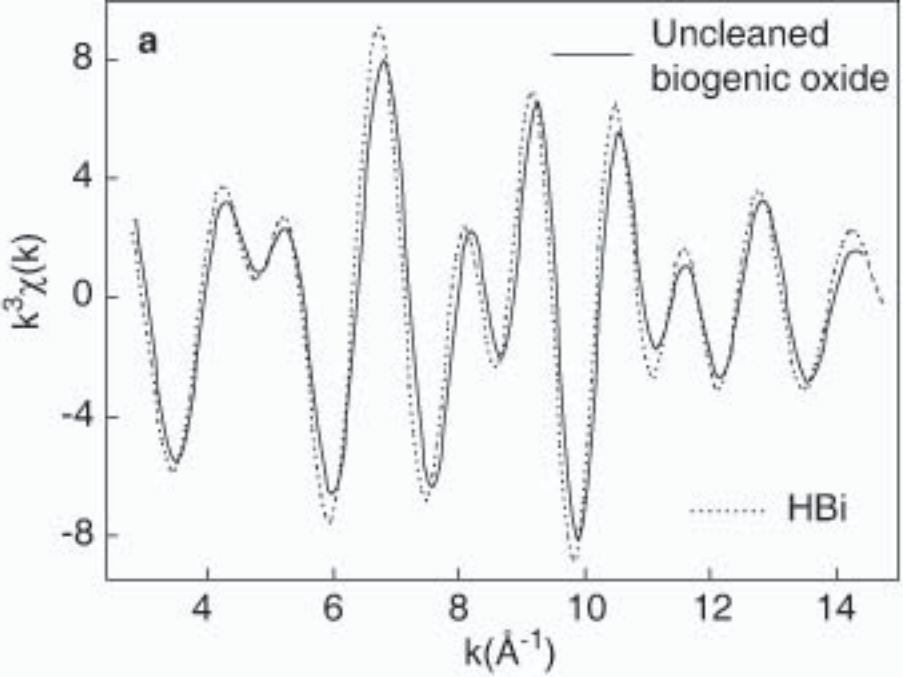

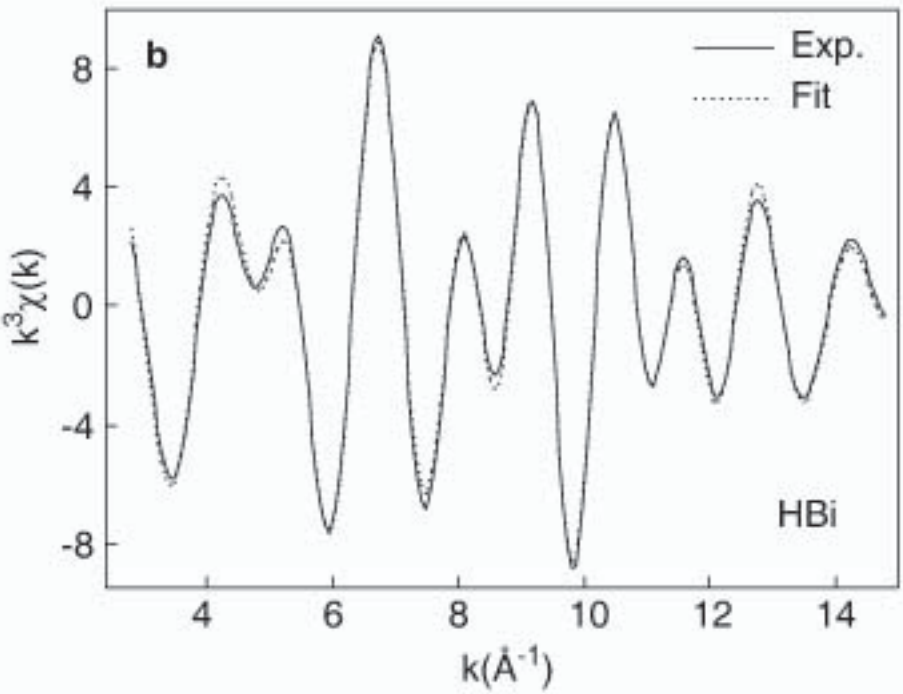

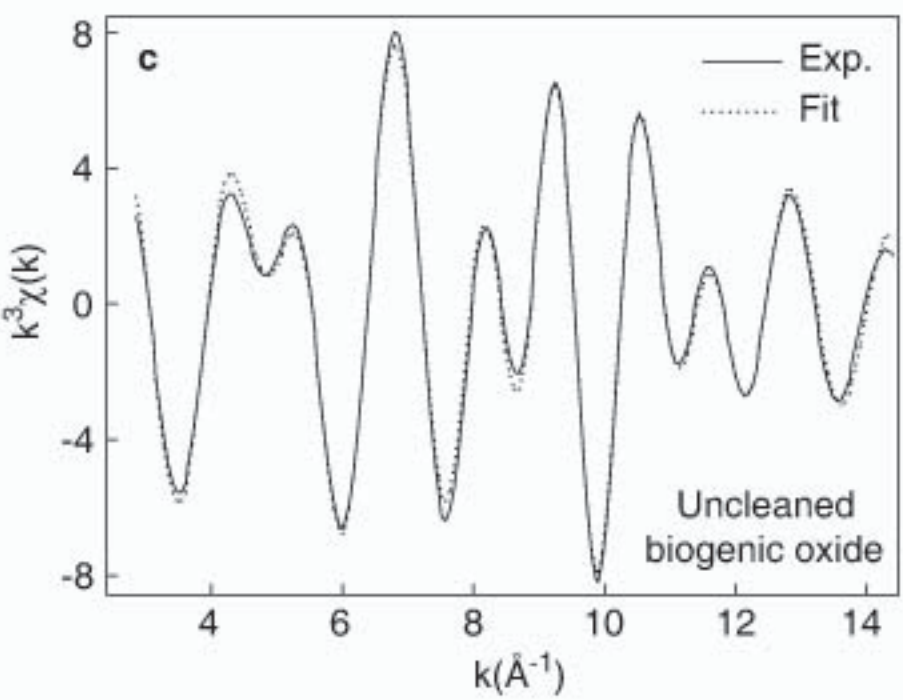

Villalobos et al., Fig_14

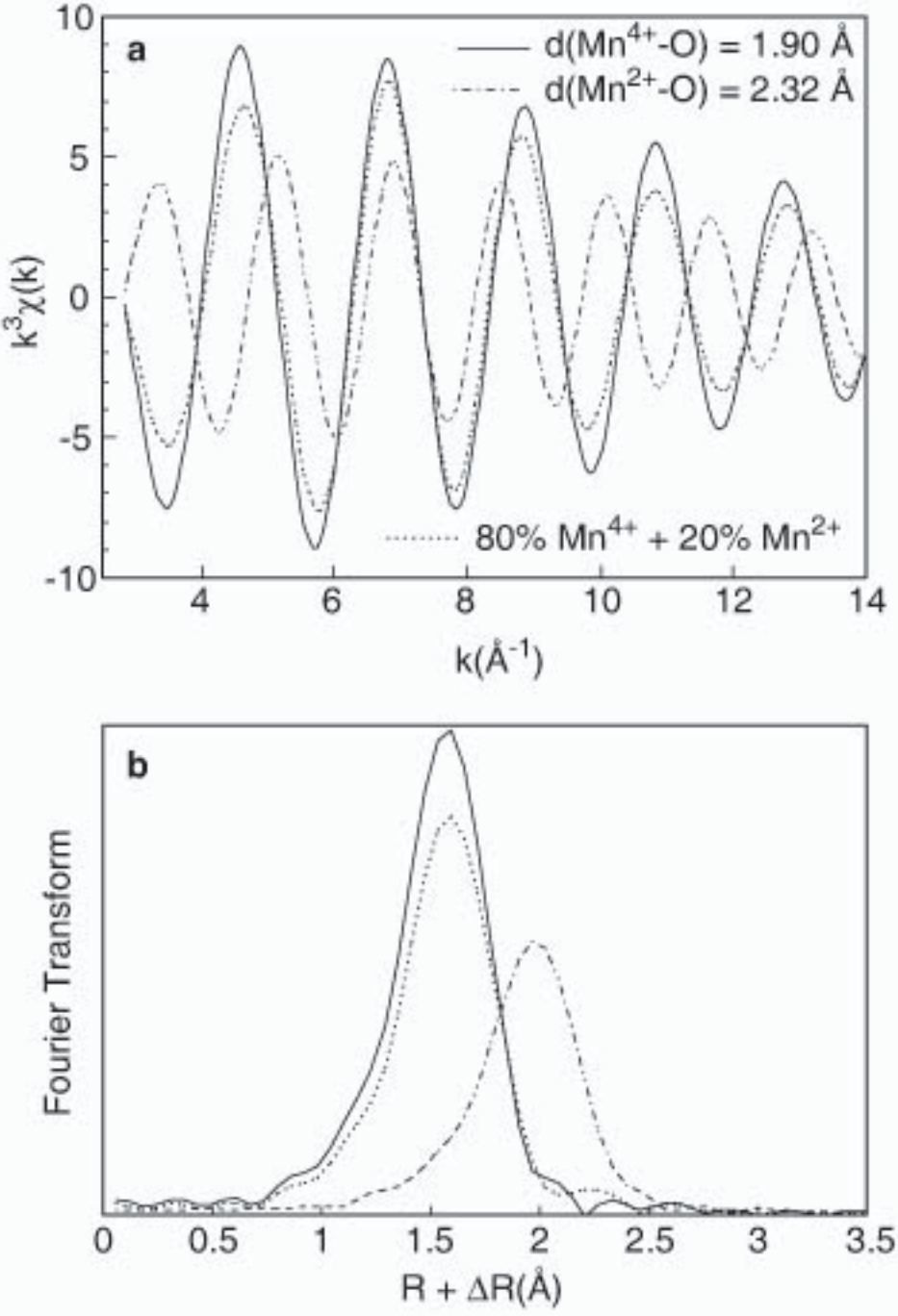
a
d(Mn4+-O) = 1.90 Å
d(Mn2+-O) = 2.32 Å
80% Mn4+ + 20% Mn2+
k3χ(k)
k(Å-1)
10
5
0
-5
-10
4
6
8
10
12
14

b
Fourier Transform
R + ΔR(Å)
0
0.5
1
1.5
2
2.5
3
3.5